EFFECTS OF CONVECTIVE ICE EVAPORATION ON WATER VAPOR INTERANNUAL VARIABILITY IN THE TROPICAL TROPOPAUSE LAYER (TTL)

A Dissertation

by

HAO YE

Submitted to the Office of Graduate and Professional Studies of
Texas A&M University
in partial fulfillment of the requirements for the degree of

DOCTOR OF PHILOSOPHY

Chair of Committee,	Andrew E. Dessler
Committee Members,	Kenneth P. Bowman
	Ping Yang
	Courtney Schumacher
	Robert Hetland
Head of Department,	Ping Yang

May 2018

Major Subject: Atmospheric Sciences

Copyright 2018 Hao Ye

ABSTRACT

The objective of this dissertation is to investigate the physical processes controlling the spatial distribution of water vapor in the tropical tropopause layer (TTL) and the impact of convective ice evaporation on TTL water vapor using a forward domain-filling trajectory model. With large-scale circulation and temperature fields, the trajectory model is able to accurately reproduce the TTL water vapor patterns of the satellite observations and climate model simulations. Comparison of TTL water vapor simulations from the trajectory model to Aura Microwave Limb Sounder (MLS) observations and climate model simulations indicates that, over decadal periods, TTL water vapor variations are primarily controlled by variability of TTL temperature. On longer century timescales, the evaporation of convective ice plays an important role and contributes to more than half of the total trend of TTL water vapor in the 21st century.

We investigate the impact of the Brewer-Dobson circulation (BDC), the quasi-biennial oscillation (QBO), and the tropospheric temperature (ΔT) on the spatial distribution of TTL water vapor using a multivariate linear regression model to decompose TTL water vapor variability. We find that the BDC and QBO affect TTL water vapor mainly by changing TTL temperatures. But for ΔT, we find that the impact on TTL water vapor cannot be explained through the TTL temperatures alone. We hypothesize a moistening role for the evaporation of convective ice from increased deep convection as the troposphere warms. Parallel analysis using a climate-chemistry model, the GEOSCCM, supports that variability in the evaporation of convective ice plays a role in water vapor variability in the TTL.

ACKNOWLEDGMENTS

I would like to thank my advisor, Dr. Andrew E. Dessler for his kind guidance and support during my Ph.D. years. His profound knowledge and quick thinking always lead me to the right path in the research and study. The working experience with Dr. Dessler has been inspiring and priceless.

I would also like to thank my committee members, Dr. Kenneth P. Bowman, Dr. Ping Yang, Dr. Courtney Schumacher, and Dr. Robert Hetland, for their kind help and valuable suggestions during my Ph.D. studies. Dr. Bowman provides me his trajectory code, which is the core method in this study. Besides, I also appreciate the suggestions and help from Dr. Mark Schoeberl, Dr. Sean Davis, Dr. Gerald R. North, Dr. Luke Oman, Dr. Anne Douglass, and Dr. Tao Wang.

I would like to thank my friends and colleagues in the department. Thank Neil Smith and Jason Root for their endless IT supports, thank Theresa Morrison, Brady Dennis, Wyatt Buchanan, Irene Martinez, and Debbie Odstrcil, etc. for their kind help in the department. I want to thank my group mates, John Kummer, Kevin Smalley, Xun Wang, Wandi Yu, Brooke Adams, and Jeffrey Mast who provide valuable discussions and suggestions.

Lastly, I would give my great thanks to my parents, my sisters, and my girlfriend for their endless love and supports all through these years.

This work was supported by NASA grants NNX14AF15G and 80NSSC18K0134 to Texas A&M University.

CONTRIBUTORS AND FUNDING SOURCES

Contributors

This work was supported by a dissertation committee consisting of Professor Andrew E. Dessler and Professors Kenneth P. Bowman, Ping Yang, and Courtney Schumacher of the Department of Atmospheric Sciences and Professor Robert Hetland of the Department of Oceanography.

The simulation of GEOSCCM used in this dissertation was provided by Dr. Luke Oman and Dr. Anne Douglass. The GEOSCCM convective evaporation rate analyzed for Chapter 4 was provided by Wandi Yu of the Department of Atmospheric Sciences.

All other work conducted for the dissertation was completed by the student independently.

Funding Sources

Graduate study was supported by NASA grants NNX14AF15G and 80NSSC18K0134 to Texas A&M University.

NOMENCLATURE

ACE-FTS	Atmospheric Chemistry Experiment Fourier Transform Spectrometer
BDC	Brewer-Dobson Circulation
CEP	Central Equatorial Pacific
CPT	Cold-point tropopause
ECMWF	European Centre for Medium-Range Weather Forecasts
ENSO	El Niño-Southern Oscillation
EOS	Earth Observing System
ERAi	ECMWF ReAnalysis interim
ERBS	Earth Radiation Budget Satellite
GEOSCCM	Goddard Earth Observing System Chemistry Model
HALOE	Halogen Occultation Experiment
ISS	International Space Station
IWC	Ice water content
LZRH	Level of zero radiative heating
MERRA	Modern-Era Retrospective-Analysis for Research and Applications
WMO	World Meteorological Organization
MLS	Microwave Limb Sounder

NCEP	National Centers for Environmental Prediction
PV	Potential vorticity
QBO	Quasi-Biennial Oscillation
SAGE	Stratospheric Aerosol and Gas Experiment
TTL	Tropical tropopause layer
TWP	Tropical warm pool
UTLS	Upper troposphere and lower stratosphere
ΔT	Tropospheric trmperature

TABLE OF CONTENTS

Page

LIST OF FIGURES

FIGURE Page

LIST OF TABLES

TABLE Page

1. INTRODUCTION

The tropical tropopause layer (TTL) serves as a transition layer between the troposphere and stratosphere in the tropics and plays a very important role in the Earth's energy balance and atmospheric mass transport. Water vapor in the TTL has a direct radiative forcing, influencing the global climate system. Thin cirrus clouds in the TTL also have a significant impact on the global energy budget. It is crucial to understand the distribution and variations of TTL water vapor as well as the physical processes controlling it.

1.1 Tropical Tropopause Layer

The Earth's atmosphere is a thin layer of air about 100 km in depth. In the simplest description of atmospheric structure, the lowest layer is the troposphere. Solar radiation mostly passes through the atmosphere and is absorbed by the Earth's surface. The warmed surface drives convection, or warm air rising, and this rising air cools as its pressure decreases. The rising air is balanced by descending air elsewhere. The troposphere is characterized by considerable vertical mixing, and general cooling with height, and extends to an average altitude of 17 km in the tropics and less than 10 km near the poles. Greenhouse gases, mainly carbon dioxide (CO_2) and water vapor, can absorb long-wave radiation and heat up the atmosphere. As the troposphere contains 85% of the total atmospheric mass and about 99% of its water vapor, most weather phenomena occur in this layer.

The next atmospheric layer is called the stratosphere, which can be up to about 50 km in altitude and contains about 15% of the total atmospheric mass. In the stratosphere, the air is stratified in temperature and often becomes warmer with height, and the vertical mixing is much weaker than in the troposphere. The warming with height is caused by absorption of solar ultraviolet radiation in the ozone layer.

The tropopause is traditionally regarded as a discrete boundary level that separates the troposphere and stratosphere, and several definitions are used in the literature. The standard lapse rate tropopause, or the thermal tropopause, is defined by the World Meteorological Organization (WMO) as "the lowest level at which the lapse rate decreases to 2 $\mathrm{K\,km^{-1}}$ or less, provided that the average lapse rate between this level and all higher levels within 2 km does not exceed 2 $\mathrm{K\,km^{-1}}$" (e.g. WMO, 1986; Holton et al., 1995). The cold-point tropopause (CPT) is defined as the level of the coldest temperature in the vertical profile (Highwood and Hoskins, 1998). The dynamical tropopause is based on potential vorticity (PV) and is defined by various researchers as the surface in extropical regions with a PV value somewhere between 1 and 5 PVU (potential vorticity unit, 1 PVU = $10^{-6}\ \mathrm{m^2\,s^{-1}\,K\,kg^{-1}}$) and usually 2 PVU (e.g. Hoskins et al., 1985; Holton et al., 1995). The dynamical tropopause within about 10° of the equator corresponds roughly to an isentropic layer, with a annual mean potential temperature about 380 K (Holton et al., 1995). All these definitions treat the tropopause as a boundary surface separating the troposphere and stratosphere.

Often a single profile contains two or more tropopause levels. The WMO definition above, in a more complete form, allows a second tropopause if there is a

layer at least 1 km deep above the first tropopause with a lapse rate averaging at least 3 $\mathrm{K\,km^{-1}}$, if the lapse rate above the 1-km layer again decreases to a less than 2 $\mathrm{K\,km^{-1}}$ average in a layer at least 2 km thick. Studies of atmospheric properties between multiple tropopauses show mixed tropospheric and stratospheric characteristics, so the concept of a tropopause in recent decades has gradually changed from a boundary level to a transition layer over the past decades (Sherwood and Dessler, 2000; Fueglistaler et al., 2009), which can be several kilometers thick.

The TTL is usually defined as the layer in the tropics running roughly from 150 to 70 hPa in pressure, from 14 to 18.5 km in altitude, and from 355 to 425 K in potential temperature (right part of Fig. 1.1) (Fueglistaler et al., 2009). The TTL is bounded in latitude by the subtropical jet, which is usually between 30°N and 30°S, where the strong westerly wind and gradients in PV weakens the poleward horizontal transport (Haynes and Shuckburgh, 2000). In Fig. 1.1, the clear-sky level of zero net radiative heating (LZRH), which is slightly higher than the bottom of the TTL, i.e., 150 hPa, separates the air into two parts. Below the LZRH, the air is radiatively cooling and is balanced by the ascent from moist convection in the troposphere. Above the LZRH, the air is radiatively heating and is balanced by ascent driven by extratropical waves. Most tropospheric convection outflow occurs below the bottom of the TTL. Only a small fraction of deep convective events penetrate the LZRH level into the TTL and the maximum convective height is usually regarded the upper boundary of the TTL (Highwood and Hoskins, 1998; Fueglistaler et al., 2009). Above the TTL, i.e., 70 hPa, the stratosphere over the tropics is isolated within what is referred to as the "tropical pipe" (Plumb, 1996) and is usually called the "overworld" (Hoskins, 1991).

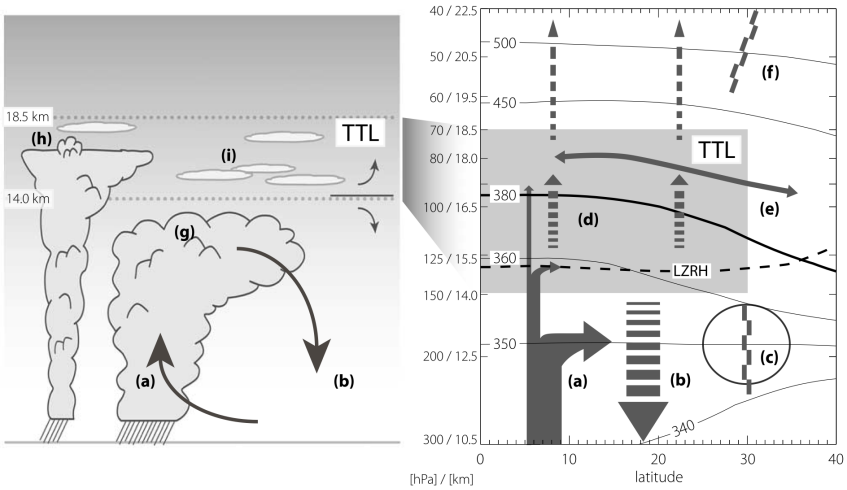

Figure 1.1: Schematic (left) of cloud processes and transport and (right) of zonal mean circulation. Arrows indicate circulation, black dashed line is clear-sky level of zero net radiative heating (LZRH), and black solid lines show isentropes (in K, based on European Centre for Medium Range Weather Forecasts 40-year reanalysis (ERA-40)). The letter a indicates deep convection: main outflow around 200 hPa, rapid decay of outflow with height in tropical tropopause layer (TTL), and rare penetrations of tropopause. Fast vertical transport of tracers from boundary layer into the TTL. The letter b indicates radiative cooling (subsidence). The letter c indicates subtropical jets, which limit quasi-isentropic exchange between troposphere and stratosphere (transport barrier). The letter d indicates radiative heating, which balances forced diabatic ascent. The letter e indicates rapid meridional transport of tracers and mixing. The letter f indicates the edge of the "tropical pipe", relative isolation of tropics, and stirring over extratropics ("the surf zone"). The letter g indicates deep convective cloud. The letter h indicates the convective core overshooting its level of neutral buoyancy. The letter i indicates ubiquitous optically (and geometrically) thin, horizontally extensive cirrus clouds, often formed in situ. The height-pressure-potential temperature relations are based on tropical annual mean temperature fields, with height values rounded to the nearest 0.5 km. Reprinted with permission from Fueglistaler et al. (2009), Copyright (2009) by the American Geophysical Union.

The TTL has features both of the troposphere and stratosphere and serves as a transition layer between the troposphere and stratosphere. Because of this, many tracer gas species, such as water vapor and ozone, show large vertical gradients in the TTL. Besides, the water vapor enters the stratosphere mainly from tropics (Brewer, 1949). It is important to investigate the vertical structure as well as the mass transport of those tracer gas species.

1.2 Water Vapor in the TTL

Water vapor plays an important role in both the chemical processes (Stenke and Grewe, 2005) and the radiative energy budget (e.g. Solomon et al., 2010; Dessler et al., 2013) of the atmosphere. Water vapor is involved in chemical reactions related to ozone in the stratosphere that have contributed to extensive ozone loss since about 1980 (Kirk-Davidoff et al., 1999; Anderson et al., 2012). Because the TTL has little water vapor, the radiation balance is very sensitive to the TTL water vapor concentration. A small change in the TTL water vapor concentration can cause a large change in the radiative energy balance, leading to a significant change in the climate. Furthermore, as a greenhouse gas, stratospheric water vapor may provide a positive climatic feedback, i.e., increases in surface temperature lead to increases in stratospheric water vapor, which in turn lead to further warming of the climate (Dessler et al., 2013).

1.2.1 Sources of TTL Water Vapor

In the stratosphere, water vapor has two main sources: oxidation of methane in the upper stratosphere, and direct transport of moist air from the troposphere. In the tropics, these two sources have different impacts on the vertical profile of stratospheric water vapor. Direct transport of tropospheric air, driven by the wave-induced Brewer-Dobson circulation (BDC), has maximum impact on water vapor in the TTL and lower stratosphere, while methane oxidation has a maximum impact on upper stratospheric water vapor. In the TTL, water vapor enters mainly by

direct transport of moist air from the troposphere, and little methane oxidation has occurred in this layer (Dessler et al., 2014).

1.2.2 Physical Processes Controlling TTL Water Vapor

Air travels from the tropical troposphere into the "overworld" stratosphere mainly through the TTL (Brewer, 1949; Dobson, 1956) through the BDC (Murgatroyd and Singleton, 1961). Observations of stratospheric water vapor mixing ratio show that the very dry stratospheric air is not likely corresponding to local CPT temperature (Mastenbrook, 1974; Kley et al., 1979) and the air enters stratosphere from troposphere at appropriate places and times (Robinson, 1980; Newell and Gould-Stewart, 1981).

It is generally recognized that the cold-point temperature in the TTL serves as a "cold trap" that controls the amount of water vapor entering the lower stratosphere (Holton and Gettelman, 2001; Fueglistaler et al., 2009). Fig. 1.2 shows the vertical distribution of zonal mean water vapor mixing ratio from the Microwave Limb Sounder (MLS) on the Aura satellite (Waters et al., 2006; Read et al., 2007). The average water vapor mixing ratio shows a large vertical gradient, from more than 400 ppmv in the upper troposphere to less than 10 ppmv just above the CPT (the dashed line in Fig. 1.2). This vertical gradient is correlated with the distribution of temperature (solid lines in Fig. 1.2) and the coldest temperature is located around and above the CPT, where the driest air in the upper troposphere and lower stratosphere (UTLS) is found. Since the CPT can be colder than -90 $^{\circ}$C, water vapor mixing ratios under 2 ppmv are occasionally found in the stratosphere.

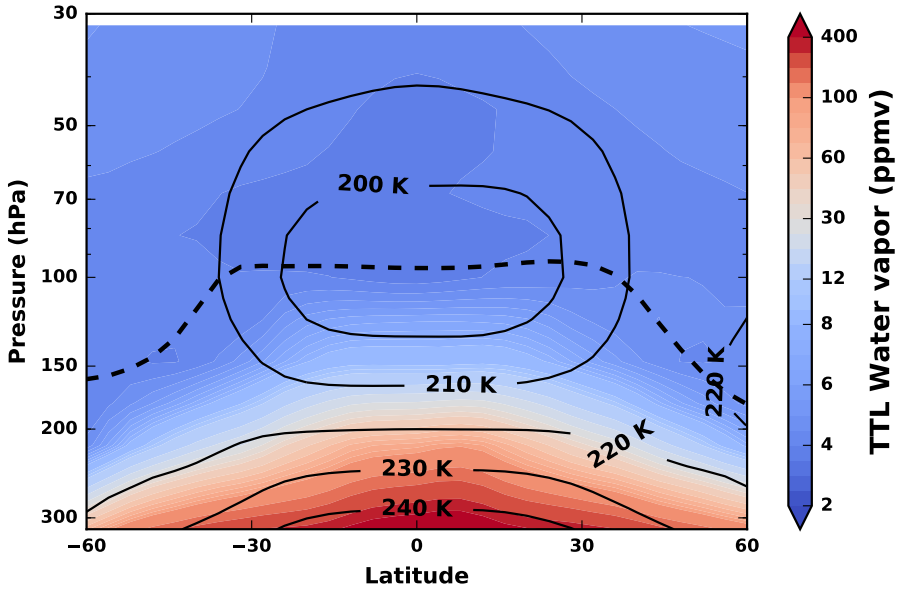

Figure 1.2: Zonal mean water vapor mixing ratio in the upper troposphere and lower stratosphere (UTLS) from MLS observations averaged from 2005 to 2016. The black dashed line is the average cold-point tropopause (CPT), and the solid lines are the zonal mean temperature. The temperature data is from ERAi.

The seasonal cycle of the TTL temperature controls the saturation mixing ratio of air transported into the lower stratosphere, leading to a seasonal cycle in stratospheric water vapor, now called the tropical tape recorder (Mote et al., 1996; Fueglistaler et al., 2009). This tape recorder signal from water vapor can be used to track stratospheric air back to where and when that air entered the stratosphere. Besides the seasonal cycle, large interannual variations of TTL water vapor have been observed and are attributed to a set of physical processes that affect water vapor by varying TTL temperatures.

The TTL temperature is anti-correlated with the strength of the BDC. The TTL temperature is cold when the BDC is strong, and vice versa (Yulaeva et al., 1994).

This correlation between the TTL temperature and the BDC also influences the TTL water vapor mixing ratio. Previous studies have shown that the variability of BDC strength is coupled to the variability in TTL water vapor, both in the seasonal cycle and the interannual variability (Yulaeva et al., 1994; Rosenlof, 1995; Randel et al., 2006; Davis et al., 2013; Dessler et al., 2013, 2014).

It is also well recognized that the quasi-biennial oscillation (QBO) drives interannual variations in TTL water vapor. The QBO impacts TTL temperatures through the secondary meridional circulation of the QBO (Giorgetta and Bengtsson, 1999). Randel et al. (2000) showed that the QBO accounts for most of the zonal mean interannual variation in the TTL temperature based on radiosonde observations. Geller et al. (2002) showed that the QBO causes interannual variations of TTL water vapor, but the QBO effect is too small to account for all observed variations. Fueglistaler and Haynes (2005) stated that the QBO has an impact on the pattern of interannual TTL temperature variability and therefore, the water vapor pattern. Recent studies (Davis et al., 2013; Tao et al., 2015; Dessler et al., 2013, 2014) also indicated that the QBO has a strong effect on the interannual variability of TTL water vapor.

Tropospheric variations also have impacts on the temperature and water vapor in the TTL. The El Niño-Southern Oscillation (ENSO) is the leading mode of variability in the tropical troposphere. The distribution of convection varies with ENSO, which could lead to interannual variability in TTL temperatures and water vapor (Gettelman et al., 2001; Fueglistaler and Haynes, 2005). However, ENSO mainly causes changes in the meridional location of the TTL temperature cold pool between El Niño and La Niña, so the variations mostly cancel out in the zonal mean (Davis et al., 2013; Hu et al., 2016; Konopka et al., 2016). Shepherd (2002)

hypothesized that a warmer troposphere leads to a warmer and higher tropopause based on a conceptual model, and this hypothesis was also confirmed in both observations (Seidel and Randel, 2006) and model simulations (Santer et al., 2003). Recent climate model simulations (Gettelman et al., 2009; Kim et al., 2013) all projected a warmer tropopause under a warming climate over the twenty-first century. Lin et al. (2017) further demonstrated TTL warming in response to tropospheric warming, due to the radiative warming from a warmer troposphere. Dessler et al. (2013, 2014) introduced the tropical averaged tropospheric temperature as an index for the impact of tropospheric climate on TTL water vapor, and demonstrated that the changes in tropical averaged tropospheric temperature can alter TTL water vapor in systematic ways.

Another important process is deep convection that reaches and penetrates the TTL. Convective ice clouds can have important impacts on the planetary energy balance (Lee et al., 2009; Zhou et al., 2014), and evaporation of the lofted ice can moisten the TTL and tropical lower stratosphere (Corti et al., 2008; Wang and Dessler, 2012). The efficiency of convective cloud evaporation is strongly related to the ambient relative humidity (Dessler and Sherwood, 2004; Wright et al., 2009) because high relative humidity inhibits evaporation. Recent aircraft measurements (Anderson et al., 2012; Herman et al., 2017) and satellite observations (Dessler and Sherwood, 2004; Sun and Huang, 2015; Schwartz et al., 2013) confirmed that deep convection enhances the lower stratospheric water vapor over the North American summer monsoon region, where relative humidity is very low.

In the tropics, the influence of convection on observed water vapor amounts is less clear. It seems certain that convective ice evaporation at least occasionally

moistens the stratosphere (Khaykin et al., 2009; Hassim and Lane, 2010; Carminati et al., 2014; Frey et al., 2015; Virts and Houze, 2015), but the impact of convection there is muted because the relative humidity of the TTL is high, suppressing evaporation, and only convection reaching above the cold point is likely to significantly impact the humidity of the stratosphere (Dessler et al., 2007).

The above discussion has shown that the TTL water vapor distribution is controlled by complicated physical processes. To the first order, the TTL temperature dominates the TTL water vapor, both on the seasonal cycle and in interannual variations. However, the variability in TTL water vapor, especially the interannual variability, cannot be explained only with the TTL temperature. Understanding these physical processes is the main objective of this study and will be further discussed in following sections.

1.3 Important Questions

This dissertation will investigate two main questions about TTL water vapor:

- What controls the spatial distribution of TTL water vapor?
- What is the impact of convective ice evaporation on TTL water vapor?

As mentioned in section 1.2.2, many studies have investigated multiple physical processes controlling the abundance of water vapor in the TTL throughout the tropics, such as the TTL temperature, BDC, QBO, and the tropospheric temperature. A more detailed investigation of the physical processes controlling the spatial distribution of the interannual variations of water vapor in the TTL is needed, focusing

particularly on the influence of evaporation of convective ice.

In this dissertation, we try to analyze the spatial distribution of TTL water vapor by comparing satellite observations and trajectory model simulations. This leads to two more specific technical questions:

- How well does the trajectory model simulate the observed water vapor in the TTL?
- What is the best way to add convective ice evaporation to the trajectory model?

These questions are investigated in the following sections.

1.4 Outline of Dissertation

The global radiation balance is very sensitive to the TTL water vapor concentration due to the low abundance and large vertical gradient of water vapor in the TTL. An understanding of TTL water vapor needs an investigation of the physical processes controlling the abundance of water vapor in TTL. This dissertation investigates in more detail the physical processes controlling the spatial distribution of interannual variations of water vapor in the TTL, particularly the influence of evaporation of convective ice.

In Chapter 2, we introduce the TTL water vapor data and trajectory model used in this dissertation. TTL water vapor data from satellite observations and a global chemistry-climate model are presented. For model simulations, we use a forward

domain-filling trajectory model driven by large-scale winds and temperature fields from reanalysis datasets.

Chapter 3 compares TTL water vapor from observations and trajectory model simulations, and investigates aspects of seasonal and interannual variations as well as the spatial distributions of TTL water vapor. Using the trajectory model, we are able to capture most of the interannual variations of TTL water vapor. A comparison of TTL water vapor from a global chemistry-climate model and the trajectory model indicates that the trajectory model also captures most characteristics of the TTL water vapor.

In Chapter 4, a simple multi-variate linear regression statistical model is applied at individual grid points over the tropics to decompose the TTL water vapor interannual variability into the dominant physical processes known to drive water vapor, i.e., BDC, QBO and tropospheric temperature. This analysis shows that the impacts from the BDC and QBO act on TTL water vapor by changing the TTL temperature. For tropospheric temperature, TTL temperatures alone cannot explain the influence on TTL water vapor. The evaporation of convective ice from increased deep convection as the troposphere warms is able to moisten the TTL.

In Chapter 5, we summarize the main conclusions and provide some thoughts on future work.

2. TTL WATER VAPOR OBSERVATIONS AND MODEL SIMULATIONS

TTL water vapor is observed globally by satellites in polar-orbit trajectories, overcoming the spatial and temporal restrictions of in situ measurements. These satellite observations have provided detailed water vapor vertical structures, seasonal and interannual variations, and multi-decade trends. Another global water vapor data source is model simulations. With proper dynamical and physical schemes, a global model can provide good long-term global water vapor simulations. In this chapter, we will first describe satellite observations of TTL water vapor. Then, a forward domain-filling trajectory model is introduced, which is intended to simulate the observed TTL water vapor. We also summarize the TTL water vapor simulations from a global chemistry-climate model.

2.1 TTL Water Vapor Observations

2.1.1 MLS Water Vapor

Water vapor has been observed continuously and globally by several satellites, from the Stratospheric Aerosol and Gas Experiment II (SAGE II) aboard the Earth Radiation Budget Satellite (ERBS) in 1984 to the very recent SAGE III aboard the International Space Station (ISS) in 2017. During these years, several remote-sensing instruments were used to obtain the water vapor in the upper troposphere and stratosphere. These instruments include the SAGE II (1984-2005) (Chu et al., 1989), the Halogen Occultation Experiment (HALOE, 1991-2005) (Russell

et al., 1993), the Atmospheric Chemistry Experiment Fourier Transform Spectrometer (ACE-FTS, 2004 to present) (Bernath et al., 2005) and the Microwave Limb Sounder (MLS) on the Aura satellite (2004-present) (Waters et al., 2006; Read et al., 2007).

MLS was launched aboard the Earth Observing System (EOS) satellite Aura in 2004 (Read et al., 2007; Lambert et al., 2007). MLS measures microwave thermal emission from the limb of Earth's atmosphere and has obtained around 3500 vertical profiles of atmospheric gases, temperature, pressure, water vapor, and cloud ice each day in the upper troposphere and stratosphere since August 2004. The data is available from https://mls.jpl.nasa.gov/.

Here we use MLS version 4 (v4.2) level 2 water vapor retrievals from August 2004 to December 2016. The MLS water vapor has a vertical grid of 12 levels per decade change in pressure between 316 hPa and 0.002 hPa. In the TTL, MLS provides water vapor data at 147 hPa, 121 hPa, 100 hPa and 83 hPa with vertical resolutions of 2.3-3.1 km and accuracies of 15% to 9% in the tropics (Read et al., 2007; Livesey et al., 2017). In this dissertation, we use the MLS water vapor at 100 hPa to represent TTL water vapor. The measurement uncertainty at 100 hPa is 10% in the tropics (Read et al., 2007).

The daily water vapor mixing ratio measurements are binned and averaged to produce monthly data on a $4^\circ \times 8^\circ$ latitude and longitude grid after quality control following instructions in Livesey et al. (2017). During the processing, we keep the original pressure levels in the vertical coordinate. We focus on the water vapor from 30°N to 30°S at 100 hPa.

2.1.2 Averaging Kernels

In remote sensing, the "averaging kernels" (Rodgers, 2000; Rodgers and Connor, 2003) are commonly used in retrieving a variable from a satellite sensor. An averaging kernel is a linear weighting function related to the information from radiances and an *a priori* guess. It is usually in the form of a matrix and is a measure of how the variable is sensitive to the "true" state. The MLS is a limb-sounding instrument that scans microwave emission by the atmosphere in layers near the horizon, so it provides high vertical resolution. However, because a signal from a level passes through nearby layers on its way to the satellite, a weighting function describes the contribution of each level to the signal received at the satellite.

The averaging kernel matrix $\mathbf{A}$ is defined as:

$$\mathbf{A} = \frac{\partial \hat{\mathbf{x}}}{\partial \mathbf{x}} \tag{2.1}$$

where $\hat{\mathbf{x}}$ is a vector for the retrieved MLS profile of a desired variable, and $\mathbf{x}$ is a vector for the "true" atmospheric state. The $\mathbf{x}$ and $\hat{\mathbf{x}}$ vectors are usually profiles of meteorological variables at specific atmospheric levels. In the averaging kernel matrix, each row gives the contributions of the true atmospheric profiles to a given retrieval level.

The averaging kernels change with the retrieval parameter species and locations. Usually this change is small with latitude in MLS. As we focus on the tropical region, in this dissertation we use a single vertical profile averaging kernel at the equator provided by the MLS data archive source. Fig 2.1 shows the averaging

kernels for MLS v4.2 water vapor at the equator at pressure levels 83 hPa (green), 100 hPa (blue), and 121 hPa (red).

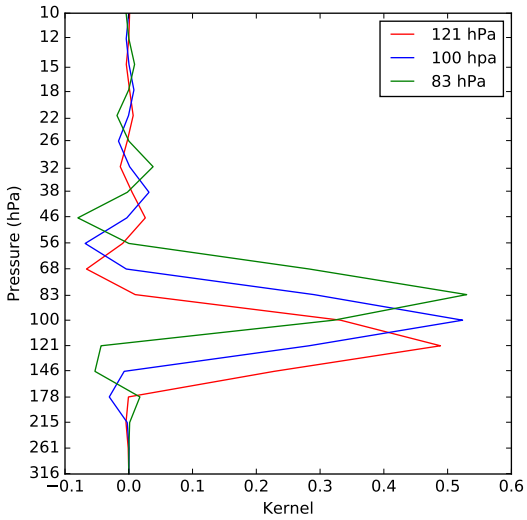

Figure 2.1: Averaging kernels for the MLS v4.2 water vapor data at the equator at the levels: 83 hPa (green), 100 hPa (blue), and 121 hPa (red).

In practice, to make the model estimates of the water vapor profile comparable to MLS observations, we need to apply the averaging kernels as:

$$\hat{\mathbf{x}} = \mathbf{x_a} + \mathbf{A}[\mathbf{x} - \mathbf{x_a}] \tag{2.2}$$

where vector $\mathbf{x}$ is a profile from model estimates of water vapor and vector $\mathbf{x_a}$ is the *a priori* profile. The *a priori* profile is provided by MLS accompanying with each MLS observation. On the left hand, the vector $\hat{\mathbf{x}}$ is the profile that MLS would observe. In eq. 2.2, each water vapor quantity is expressed as the logarithm of

the water vapor mixing ratio in $\mathbf{x}$, $\mathbf{x_a}$, and $\hat{\mathbf{x}}$ as the saturation mixing ratio varies approximately exponentially with the frost point temperature. After this procedure, the profiles from model simulations can be compared to the corresponding profiles from MLS observations.

2.2 Trajectory Model

In fluid dynamics, a Lagrangian trajectory model is usually used to follow the flow because it is the most efficient way to investigate the motion and transport in the atmosphere. In the Lagrangian system, the atmosphere is treated as an assembly of massless and dimensionless parcels. Every parcel is independent from the others and moves following the macroscopic wind, resulting in non-diffusive transport. This is especially beneficial in regions with large tracer gradients, such as the TTL and UTLS. Another benefit of the Lagrangian trajectory model is that through the trajectory, we can track the whole history of the parcel both forward and backward.

In the Lagrangian trajectory model, the trajectory of a parcel is calculated following the motion using this equation:

$$\frac{\mathrm{d}\mathbf{x}}{\mathrm{d}t} = \mathbf{v}(\mathbf{x}(t), t), \quad \mathbf{x}(t_0) = \mathbf{x_0} \tag{2.3}$$

where $\mathbf{x}(t)$ is the trajectory location of the parcel after the transport following the winds with a speed of $\mathbf{v}(\mathbf{x}(t), t)$ and $\mathbf{x_0}$ is the initial position of the parcel. Once knowing the wind speed $\mathbf{v}(\mathbf{x}(t), t)$ and initial position $\mathbf{x_0}$, we can obtain the path of the parcel with a proper integration scheme to solve equation 2.3, which is an

ordinary differential equation.

2.2.1 Forward Domain-filling Trajectory Model

In this dissertation, the trajectory model uses Bowman's trajectory code (Bowman, 1993; Bowman and Carrie, 2002), which is based on a classic fourth-order Runge-Kutta scheme to integrate equation 2.1. The calculation of the parcel path from time t_n to next time t_{n+1}, i.e. from location $\mathbf{x}_n$ to a new location $\mathbf{x}_{n+1}$, is based on velocity $\mathbf{v}$ at four stages ($\mathbf{k}_1$, $\mathbf{k}_2$, $\mathbf{k}_3$, $\mathbf{k}_4$) and are weighted as follows:

$$\mathbf{x}_{n+1} = \mathbf{x}_n + \frac{1}{6}(\mathbf{k}_1 + 2\mathbf{k}_2 + 2\mathbf{k}_3 + \mathbf{k}_4) \cdot \delta t \tag{2.4}$$

where δt is the duration of one model time step.

The four vectors ($\mathbf{k}_1$, $\mathbf{k}_2$, $\mathbf{k}_3$, $\mathbf{k}_4$) are estimates of the parcel velocities during the time from t_n to t_{n+1} and they are calculated as:

$$\mathbf{k}_1 = \mathbf{v}(\mathbf{x}_n, t_n), \tag{2.5}$$

$$\mathbf{k}_2 = \mathbf{v}(\mathbf{x}_n + \mathbf{k}_1 \cdot \frac{\delta t}{2}, t_n + \frac{\delta t}{2}), \tag{2.6}$$

$$\mathbf{k}_3 = \mathbf{v}(\mathbf{x}_n + \mathbf{k}_2 \cdot \frac{\delta t}{2}, t_n + \frac{\delta t}{2}) \tag{2.7}$$

$$\mathbf{k}_4 = \mathbf{v}(\mathbf{x}_n + \mathbf{k}_3 \cdot \delta t, t_n + \delta t) \tag{2.8}$$

This scheme has high accuracy, and the total accumulated truncation error is on the fourth order of the time step size. In practice, the time step in the trajectory model is 45 minutes, or 32 steps per day, which is much shorter than the 6-hourly

temporal resolution of the archived wind velocity fields. The truncation error has been proved to be much smaller than the error from uncertainty in wind velocity fields, and the latter one is the majority of the error from this scheme (Bowman, 1993).

In the trajectory model simulations, there are usually two approaches for the vertical wind velocity fields. The first one is that with a pressure coordinate, the vertical velocity is defined as pressure tendency, i.e. $\omega = \frac{\mathrm{d}p}{\mathrm{d}t}$. In this approach, the parcels cross vertical isobaric levels following the vertical velocity, so these trajectory model simulations are referred to as kinematic runs. The vertical velocity in kinematic runs is derived from the mass continuity equation, and errors are mostly due to errors in the horizontal wind fields.

The other approach is to use potential temperature as the vertical coordinate with the vertical velocity defined as potential temperature tendency, i.e. $\dot{\theta} = \frac{\mathrm{d}\theta}{\mathrm{d}t}$. In potential temperature coordinates, parcels are on isentropic levels and move with the horizontal winds, but pass across isentropic levels following the potential temperature tendency. This is referred to as the diabatic approach. In this approach, the vertical velocity is calculated from the diabatic heating rate. This does not have the known disadvantages of previous kinematic approaches. Previous studies showed that diabatic runs have less vertical dispersion and more realistic parcel movements (Schoeberl et al., 2003; Ploeger et al., 2010; Schoeberl and Dessler, 2011). In this dissertation, we apply diabatic runs in the trajectory model simulations and calculate the vertical velocity from the diabatic heating rate.

In the trajectory model simulations, 1350 parcels are initialized every day from January 2000 to December 2016 on an equal area grid from 60°N to 60°S. The

parcels are released on the 370-K isentropic level, which is just above the zero net diabatic heating level over the tropics ($\sim$355-360 K) but below the cold point ($\sim$375-380 K). Each parcel travels forward following the horizontal winds and diabatic heating rate. Once a parcel has a pressure larger than 250 hPa, it is regarded as having descended back into the troposphere and is removed from the model. This process is repeated every day, and gradually the parcels will fill up the stratospheric domain. This is the concept of "domain-filling" in this trajectory model.

Each parcel is initialized with a water vapor mixing ratio of 200 parts per million by volume (ppmv). As the parcel travels upward through the CPT, the initial water vapor mixing ratio is set to guarantee the essential dehydration for the parcel. The simulated water vapor mixing ratio is insensitive to the the initial value, whenever it is more than about 20 ppmv. Along the trajectory, a parcel will immediately be dehydrated to saturation whenever its water vapor mixing ratio exceeds a predetermined saturation threshold, 100% in this study. The saturated water vapor mixing ratio is obtained from the thermodynamic equation with respect to ice (Murphy and Koop, 2005) based on temperatures. Production of water vapor from methane oxidation is also included in these trajectory model runs using a standard methane oxidation rate.

The water vapor mixing ratio from the trajectory model is gridded into $4^\circ \times 8^\circ$ bins, corresponding to the MLS bins. In the vertical, the trajectory output is binned by averaging the parcels in a pressure range around each MLS level. As introduced in section 2.1.2, the gridded water vapor mixing ratio is then re-averaged using the MLS averaging kernels to make the simulations comparable to MLS observations. When doing this kernel averaging, grid boxes with no trajectory parcels (mostly at

low altitudes) are filled with monthly water vapor mixing ratios from the reanalyses (ERAi and MERRA-2). Sensitivity tests on this will be discussed in chapter 3.

2.2.2 Trajectory Model Inputs

As introduced in section 2.2.1, the parcels in the trajectory model are driven by wind fields. In this dissertation, the wind fields are from two reanalysis datasets: the European Centre for Medium-Range Weather Forecasts (ECMWF) ERA-interim reanalysis (ERAi) (Dee et al., 2011), and the NASA Modern-Era Retrospective-Analysis for Research and Applications, Version-2 (MERRA-2) (Bosilovich et al., 2016). The data period for both reanalyses in this dissertation is from 2004 to 2016.

ERAi is based on a 12-hour 4-dimensional variational analysis on 60 vertical levels from the surface up to 0.1 hPa. The original spatial resolution of ERAi is very high with approximately 80 km (T255 spectral) grid boxes in latitude and longitude. We use 6-hourly wind products from ERAi.

MERRA-2 has a significant number of improvements over MERRA (Molod et al., 2015). The spatial resolution of MERRA-2 is $0.625^\circ \times 0.5^\circ$ with a horizontal grid of 576 points in longitude and 361 points in latitude. In the vertical direction, MERRA-2 provides variables on a native vertical grid with 72 model layers, up to 0.01 hPa. As with ERAi, we use 6-hourly wind fields in the trajectory models from MERRA-2.

For convenient use by transport models, we remapped the original 6-hourly winds to a low resolution of $2^\circ \times 2^\circ$ using bilinear interpolation while keeping the native vertical grid. Tests with different wind field resolutions show that the influ-

ence from this change in resolution on the model simulations is small.

In the vertical potential temperature coordinate, we use potential temperature tendency as the vertical wind and calculate it from the diabatic heating rate. In ERAi, the diabatic heating rate includes components from long-wave and short-wave radiations. MERRA-2 provides a total diabatic heating rate at native vertical levels from physics, including long-wave radiation, short-wave radiation, moist processes, gravity wave drag, friction, and turbulence. The horizontal winds (U, V) and diabatic heating (Q) at native vertical grid levels were linearly interpolated to isentropic layers for use by the forward diabatic trajectory model.

In addition to wind fields, we also use the 6-hourly temperature field from the reanalysis datasets. The temperature fields are also re-gridded from the original horizontal resolution to a coarser $2^\circ \times 2^\circ$ grid using bilinear interpolation, but the native vertical grid is kept. In the trajectory model, the temperatures are linearly interpolated to the parcel locations and are used to constrain the maximum water vapor mixing ratio in the parcels.

2.3 Other Data in Dissertation

2.3.1 GEOSCCM

We also use simulations of TTL water vapor from the Goddard Earth Observing System Chemistry Climate Model (GEOSCCM) for the whole 21^{st} century in this dissertation. The state-of-the-art GEOSCCM includes the GEOS-5 atmospheric general circulation model (Molod et al., 2012) with a single-moment cloud micro-

physics scheme (Bacmeister et al., 2006; Barahona et al., 2014) and the StratChem stratospheric chemical mechanism (Pawson et al., 2008; Oman and Douglass, 2014). The GEOSCCM simulation provides long term simulations of temperature, water vapor, horizontal winds, diabatic heating rates, and convective cloud ice water content with a resolution of $2^\circ \times 2.5^\circ$ in latitude and longitude on 72 vertical model levels, up to 0.01 hPa.

2.3.2 Convective Ice

We also use estimates of convective occurrence produced by combining geostationary infrared satellite imagery and rainfall measurements (Pfister et al., 2001; Bergman et al., 2012; Ueyama et al., 2014, 2015). The data have a horizontal resolution of $0.25^\circ \times 0.25^\circ$ and a temporal resolution of 3 hours and cover the period from 2005 to 2016. In the data, the cloud-top height and cloud-top potential temperature are provided and we use them to estimate the convective cloud occurrence frequency in the TTL, which we take to be an indicator of convective influence on the TTL. These data are available from https://bocachica.arc.nasa.gov/~lpfister/cloudtop/.

2.4 Summary

This chapter introduced the TTL water vapor observations from MLS used in this dissertation. We choose 100 hPa to represent the TTL in this dissertation. To compare with TTL water vapor observations, we introduced a forward domain-

filling trajectory model driven by reanalysis data, which has been verified to be able to accurately simulate water vapor variability in the TTL. Details of the comparison of TTL water vapor between observations and trajectory model simulations will be presented in the next chapter.

We also briefly introduced a state-of-the-art global chemistry-climate model (GEOSCCM), which produces continuous fields of temperature, wind, diabatic heating rate, water vapor, and convective cloud ice water content. We will also compare the TTL water vapor simulations from GEOSCCM with the trajectory model simulations driven by meteorological fields from GEOSCCM in chapter 3 to check the performance of the simple physical-based trajectory model in comparison to other detailed complex models.

3. MODEL SIMULATIONS OF TTL WATER VAPOR *

In the atmosphere, water vapor is the most abundant greenhouse gas and has a large impact on the global climate. Water vapor can absorb infrared radiation from the surface and this accounts for most of the greenhouse effect on the Earth. Besides direct warming from water vapor, the warmed troposphere from anthropogenic greenhouse gases emission can hold more water vapor, which itself is as a greenhouse gas and can lead to further atmospheric warming. This is known as the water vapor feedback mechanism. Meanwhile, the warmer troposphere leads to more and higher cirrus clouds, which are believed to have a warming effect on the climate and have positive feedback. The feedback from water vapor is mostly caused by the change of humidity in the tropical upper troposphere (Held and Soden, 2000). To obtain better knowledge of the water vapor impact on climate, it is essential to accurately simulate the water vapor in TTL.

In this chapter, we will compare the water vapor simulation from a forward domain-filling trajectory model driven by reanalysis data sets to satellite observations in the TTL. The spatial distribution, vertical distribution, seasonal cycle, and interannual variability are discussed in this chapter. A further comparison will be performed between water vapor simulations from the GEOSCCM as well as the trajectory model driven by the meteorological fields from the GEOSCCM.

*Portions of this chapter are reprinted with permission from "Transport of ice into the stratosphere and the humidification of the stratosphere over the 21st century" by A. Dessler, H. Ye, T. Wang, M. Schoeberl, L. Oman, A. Douglass, A. Butler, K. Rosenlof, S. Davis, and R. Portmann, 2016, Geophys. Res. Lett., 43, 2323–2329, Copyright [2016] by the American Geophysical Union.

3.1 Water Vapor Simulations from Trajectory Model

3.1.1 Trajectory Model Settings

The Lagrangian trajectory model has been demonstrated to be a useful method to reproduce the transport and budget of water vapor in the TTL and lower stratosphere (e.g., Schoeberl and Dessler, 2011; Schoeberl et al., 2012, 2013, 2014; Wang et al., 2014). As introduced in section 2.2.1, we use a Lagrangian domain-filling forward trajectory model in this dissertation to simulate the water vapor in the UTLS. Every day, parcels are released from the 370 K isentropic level on an equal area grid from 60°N to 60°S with 30×45 points in latitude and longitude, respectively, with an initial mixing ratio of 200 ppmv. As the parcels ascend upward toward the CPT, whose typical temperature is below -70 °C (see Fig. 1.2), the mixing ratio of the parcels is reduced due to the dehydration in TTL. Note that we remove all water vapor in excess of the saturation mixing ratio immediately and do not consider the re-evaporation of this condensed water in the lower layers. Sensitivity tests on the initial water vapor mixing ratio show that the water vapor simulations are not sensitive to the initial value as long as it is larger than the typical TTL mixing ratio of ∼20 ppmv (see Fig. 1.2).

3.1.2 Averaging Kernels

To compare the water vapor simulations from the trajectory model to satellite observations, the model's water vapor mixing ratio is averaged in a pressure range

around each MLS level. As the parcels are released at the 370 K isentropic level, $\sim$120 hPa in tropics, the trajectory model can only reasonably simulate the tropical water vapor above 100 hPa.

As mentioned in section 2.1.2, the averaging kernels need to be considered when comparing model simulations to the satellite observations from MLS. The MLS averaging kernels have coefficients for 42 levels ranged from 316 hPa to 0.002 hPa and the matrix contains the weighting function for each MLS level. We choose the averaging kernel at the equator to represent the tropics in this dissertation. All the variables used in eq. 2.2 are gridded into the same horizontal bins with $4^\circ \times 8^\circ$ in latitude and longitude, respectively. We choose water vapor at 100 hPa and 83 hPa as examples and show the weighting coefficients from 215 hPa to 56 hPa in Table 3.1. As expected, for calculation of water vapor at 100 hPa or 83 hPa, the weighting coefficient is largest at that level, i.e. coefficient of 0.52 at 100 hPa for water vapor calculation at 100 hPa.

Table 3.1: MLS averaging kernel coefficients for water vapor at 100 hPa and 83 hPa. Only 8 levels of MLS averaging kernel coefficients are shown from 215 hPa to 56 hPa, parts of the 42 levels coefficients from 316 hPa to 0.002 hPa. These coefficients are also shown in fig. 2.1 as blue (100 hPa) and green (83 hPa) lines.

	MLS levels (hPa)							
	215	178	146	121	100	83	68	56
83 hPa	0.0014	0.017	-0.053	-0.043	0.32	0.53	0.28	0.00019
100 hPa	-0.0024	-0.031	-0.0072	0.28	0.52	0.29	-0.0039	-0.068

One issue is that the trajectory model does not simulate water vapor at levels below 100 hPa, which are below the initial level of 370 K while are required for

the averaging kernels. In this dissertation, we use the water vapor specific humidity field from reanalysis data sets, i.e. ERAi and MERRA-2, for altitudes below 100 hPa when doing the kernel calculations. It has been shown that the reanalyses overestimate the water vapor in the upper troposphere (e.g. Jiang et al., 2015) and it is essential to test the impact and sensitivity of the reanalysis water vapor to trajectory model simulations.

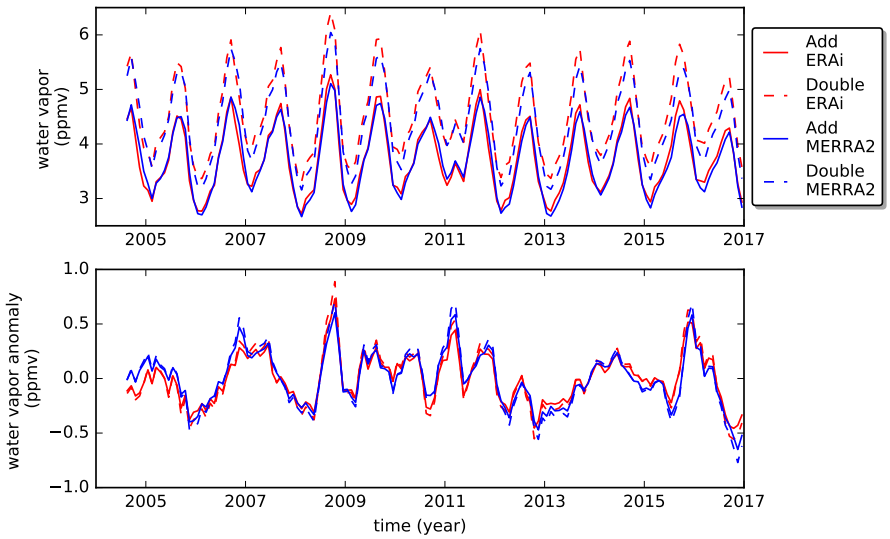

Figure 3.1: Sensitivity tests for the monthly water vapor (top) concentration and (bottom) anomaly at 100 hPa after applying MLS averaging kernels to trajectory model simulations. The solid lines use water vapor content below 100 hPa from ERAi (red) and MERRA-2 (blue) and the dashed lines use doubled water vapor content below 100 hPa. Anomalies are calculated by subtracting the mean annual cycle from the simulations.

Fig. 3.1 shows the water vapor mixing ratio at 100 hPa from trajectory model simulations after applying MLS averaging kernels. To test the sensitivity of our method to the reanalysis water products, we doubled the amount of water vapor

below 100 hPa from reanalysis data sets in eq. 2.2. From the top panel of Fig. 3.1, the model-predicted tropical average water vapor content at 100 hPa increases after doubling the water vapor from reanalysis data, with difference of about 0.6 $\sim$ 1.1 ppmv. However, while the absolute value increases, the anomalies do not (bottom panel of Fig. 3.1).

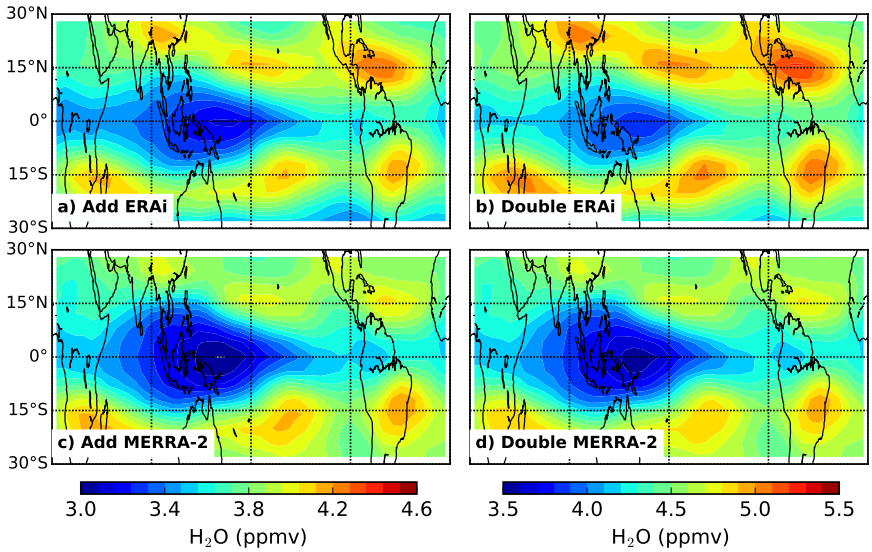

Figure 3.2: Horizontal distribution of mean water vapor mixing ratio at 100 hPa from trajectory model simulations driven by (top row) ERAi and (bottom row) MERRA-2 with applying MLS averaging kernels. Left panels: Use the water vapor content below 100 hPa from reanalysis data. Right panels: Double the water vapor content below 100 hPa.

To further test the impact of possible overestimated water vapor from reanalyses, Fig. 3.2 shows the horizontal distribution of the mean water vapor mixing ratio at 100 hPa from trajectory model simulations weighted with MLS averaging kernels. The right panels show trajectory model simulations of 100 hPa water vapor

after applying doubled water vapor from reanalyses. Although there are differences between the left and right columns, the spatial distribution pattern remains the same with lowest water vapor in the tropical warm pool (TWP) region and several high centers in subtropical regions around 15°S and 15°N.

3.1.3 Comparison with Satellite Observations

The vertical distributions of tropical average water vapor from MLS observations and the two trajectory model simulations are shown in Fig. 3.3. Here, we consider the mean water vapor in the tropics between 30°S and 30°N from August 2004 to Dec. 2016. This vertical distribution shows a clear annual cycle, which is referred to as the "tape recorder" (Mote et al., 1996). The signal shows high and low water vapor in boreal summer and winter, respectively, in the TTL due to the seasonal cycle of tropopause temperature. The slow Brewer-Dobson circulation in the stratosphere lifts the signal from 100 hPa to $\sim$40 hPa in about one year. Due to the weak vertical mixing of air, the signal persists throughout the lower stratosphere, thereby retaining the memory of tropopause variability.

Fig. 3.3 shows that the "tape recorder" in the MLS observations is similar to that in the trajectory model simulations, verifying that it is the seasonal cycle of TTL temperatures that drives the tape recorder. One clear difference is that the trajectory model generates a drier stratosphere due to the cold biased tropopause temperature in the reanalyses and neglect of high-frequency gravity waves (Schoeberl et al., 2012, 2013). Fig. 3.3b also shows that the tape recorder signal from the trajectory model driven by ERAi propagates upward too fast, due to the larger diabatic heating

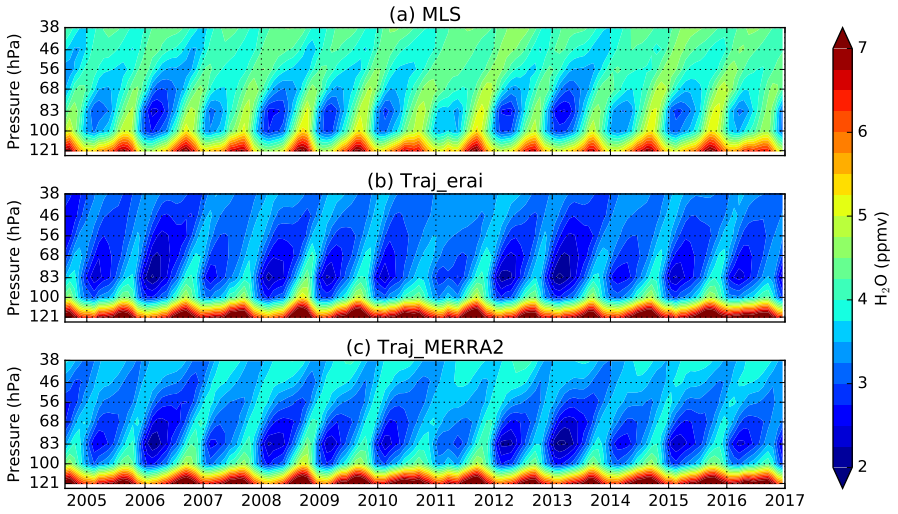

Figure 3.3: Vertical distribution of tropical average water vapor mixing ratio from (a) MLS observations, (b) trajectory model simulation driven by ERAi, and (c) trajectory model simulation driven by MERRA-2.

rate in the ERAi dataset.

In this dissertation, we choose 100 hPa as the level to investigate the TTL water vapor mixing ratio. Fig. 3.4a shows the TTL water vapor mixing ratio from MLS observations and trajectory model simulations. Similar to the tape recorder signal, the trajectory model does a good job reproducing the seasonal cycle of TTL water vapor.

We focus our analysis on the monthly anomalies, which are the remainders after the mean annual cycle from 2004 to 2016 is subtracted. Fig. 3.4b shows that the trajectory model accurately reproduces the interannual variations in TTL water vapor from the MLS observations, with correlation coefficients of 0.98 and 0.99 for trajectory model runs driven by ERAi and MERRA-2, respectively. The

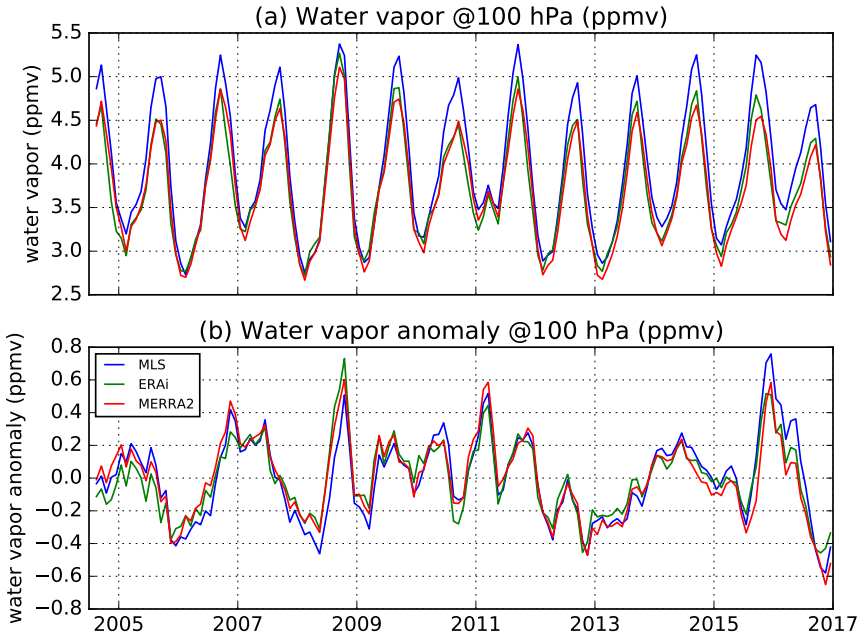

Figure 3.4: Tropical average (a) water vapor and (b) water vapor anomaly time series at 100 hPa from MLS observations (blue) and trajectory model simulations driven by ERAi (green) and MERRA-2 (red) from August 2004 to December 2016.

good agreement between observations and trajectory model simulations indicates that the tropical average TTL water vapor is primarilly controlled by the tropopause temperature, which is the only controlling factor of the amount of TTL water vapor in the trajectory model.

Fig. 3.5 compares the horizontal distribution of TTL water vapor mixing ratio as well as the temperature at 100 hPa averaged from August 2004 to 2016. The TTL water vapor is lowest in the western equatorial Pacific Ocean, where enhanced convection leads to the lowest TTL temperature. In Fig. 3.5a, the MLS observations show that the TTL water vapor has maxima over the subtropics around 15°S

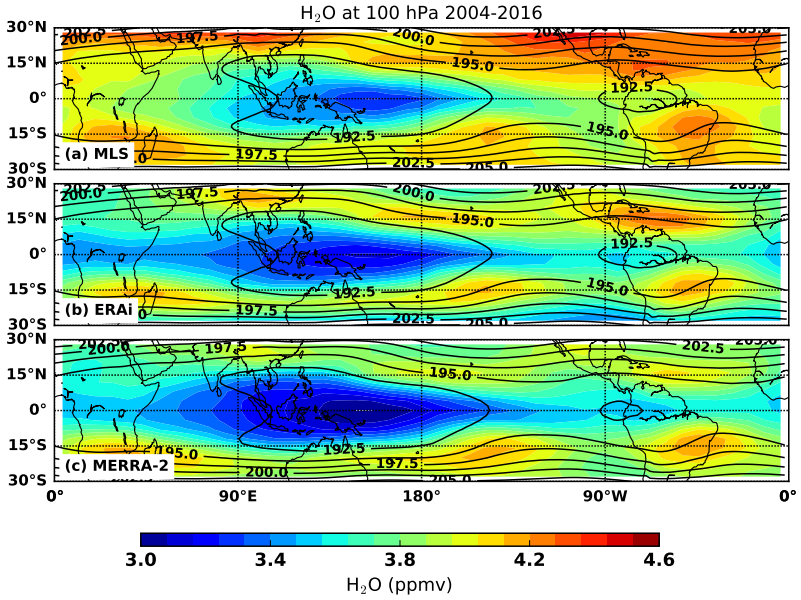

Figure 3.5: Horizontal distribution of TTL water vapor at 100 hPa between August 2004 and December 2016 from (a) MLS observations and trajectory model simulations driven by (b) ERAi and (c) MERRA-2. The contours are the temperature (K) at 100 hPa.

and 15°N, which are also captured by the trajectory model simulations shown in Figs. 3.5b and 3.5c. These centers are associated with the local high TTL temperatures. It is noteworthy that the trajectory model fails to reproduce the high values around 30°S and 30°N, especially over the Asian Monsoon and American Monsoon regions. The difference in TTL water vapor shows that the trajectory model underestimates the observations in these regions.

3.2 Comparisons with GEOSCCM

3.2.1 Motivation

In the last section, the good agreement of tropical average TTL water vapor between satellite observations and trajectory model simulations indicates that the trajectory model accurately reproduces TTL water vapor using the large scale meteorological fields from reanalyses. We confirm that variability of TTL water vapor is primarily controlled by the TTL temperature variations (e.g. Mote et al., 1996; Randel et al., 2004; Fueglistaler et al., 2005, 2009; Dessler et al., 2014).

Climate models have long simulations of TTL water vapor and nearly all predict that TTL water vapor will increase in next century (Gettelman et al., 2010; Kim et al., 2013). Most studies primarily attributed this increase in TTL water vapor to the warming of the TTL (e.g. Fueglistaler and Haynes, 2005; Oman et al., 2008; Gettelman et al., 2009; Garfinkel et al., 2013).

The trajectory model in this dissertation simulates TTL water vapor through large-scale circulation and temperature fields. If we drive the trajectory model with meteorological fields from the climate model, we can compare climate model water vapor and trajectory model water vapor, like we did with MLS observations, to evaluate the realism of the climate model.

3.2.2 Short-term Water Vapor Simulations

We first compare water vapor simulations from the trajectory model, referred as "100% traj_ccm" hereafter, and GEOSCCM from 2005 to 2016. This comparison is parallel to the comparison shown in section 3.1.3.

In addition to the trajectory model simulation introduced in section 2.2.1, we add two more trajectory model runs in the analysis. First, we change the saturation threshold in the trajectory model from 100% to 80% to test the sensitivity of the simulation to the saturation threshold because GEOSCCM begins dehydration below 100% (Molod, 2012). This one is referred to as "80% traj_ccm".

In the other simulation, we add evaporation of convective ice into the trajectory model. To do this, we use the 6-hourly three-dimensional convective cloud ice water content (IWC) field from GEOSCCM and linearly interpolate it to each parcel's position at every time step. We then assume instantaneous and complete evaporation of this ice into the parcel by adding the IWC to the parcel's water vapor, although we do not let parcels exceed 80% relative humidity with respect to ice. This one is referred as "80% traj_ccm_ice" hereafter.

Fig. 3.6 shows that the trajectory model does a good job reproducing the tape recorder signal of tropical average water vapor in GEOSCCM from 100 hPa to 40 hPa. The 100% traj_ccm and 80% traj_ccm_ice produce a wetter stratosphere, particularly in summer, while the 80% traj_ccm produces a much drier stratosphere. Despite this, the seasonal cycle is very similar in the TTL between GEOSCCM and trajectory model simulations. At altitudes below 50 hPa, the propagation of the signal shows an obvious difference, with the trajectory model lagging $\sim$2 months

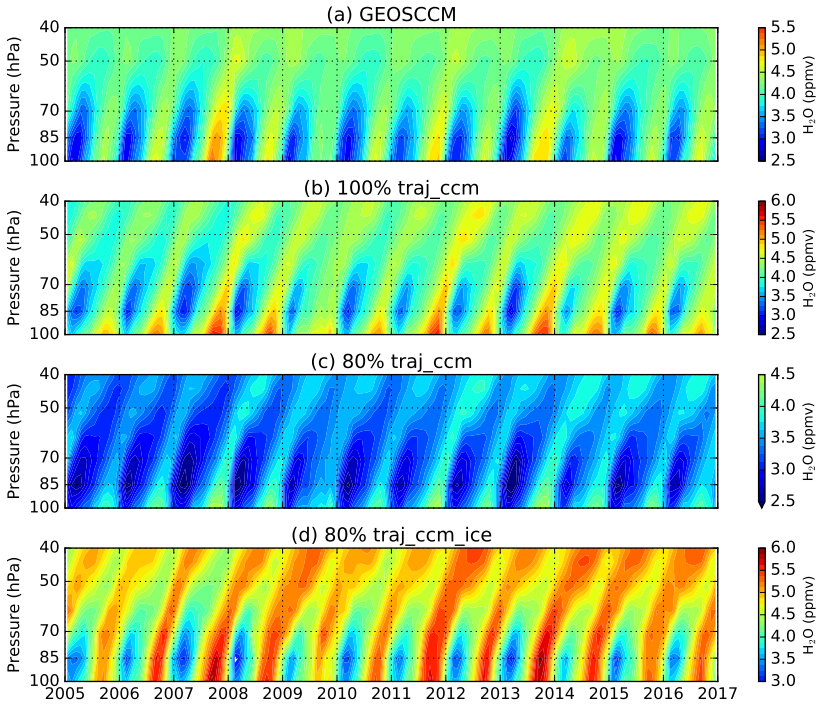

Figure 3.6: Vertical distribution of tropical average water vapor mixing ratio from (a) GEOSCCM and (b-d) three trajectory model simulations driven by GEOSCCM from 2005 to 2016. The values are averaged between 30°S and 30°N. The colors in all plots represent same values despite the different colorbars.

in comparison to GEOSCCM.

Fig. 3.7a shows the TTL water vapor from GEOSCCM and the three different trajectory model simulations. As we can see that both traj_ccm and 80% traj_ccm_ice predict much higher TTL water vapor than GEOSCCM through the time period and they show similar magnitudes of the annual cycle of TTL water vapor. On the other hand, the 80% traj_ccm underpredicts the magnitude of TTL water vapor in comparison to GEOSCCM (Oman et al., 2008; Molod et al., 2012).

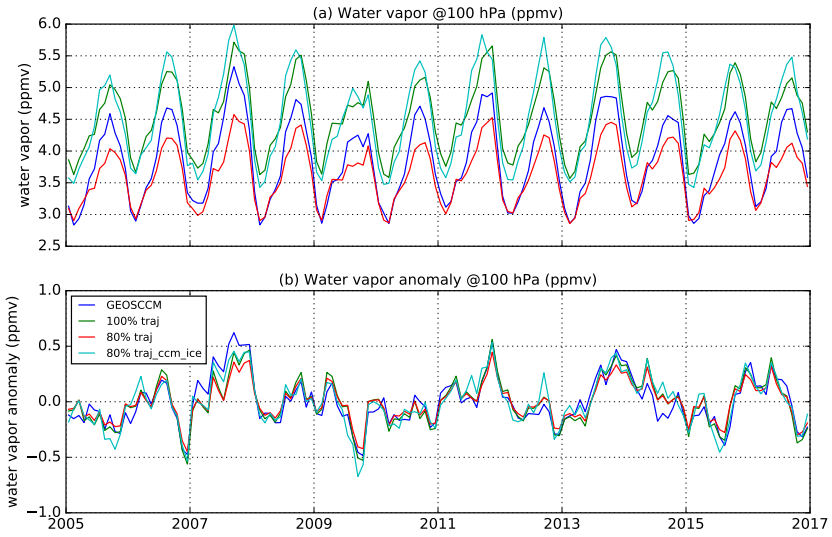

Figure 3.7: Tropical average (a) water vapor and (b) water vapor anomaly time series at 100 hPa from GEOSCCM simulations (blue) and trajectory model simulations driven by GEOSCCM from 2005 to 2016. The three trajectory model simulations are from "100% traj_ccm" (green), "80% traj_ccm" (red), and "80% traj_ccm_ice" (cyan).

This is particularly true in boreal winter, and less so in boreal summer, indicating that the trajectory model has missed some sources of water vapor in boreal summer. The annual cycle of TTL water vapor from 2005 to 2016 in Fig. 3.8 highlights this difference.

Fig. 3.7b shows that all trajectory model schemes obtain very similar tropical average TTL water vapor anomalies and agree well with the GEOSCCM, with all correlation coefficients larger than 90%. Thus, we confirm that the trajectory model can reproduce the tropical average TTL water vapor anomaly of GEOSCCM and the variability of TTL water vapor is primarily controlled by the TTL temperature.

The horizontal distribution of the TTL water vapor shows a minimum over the

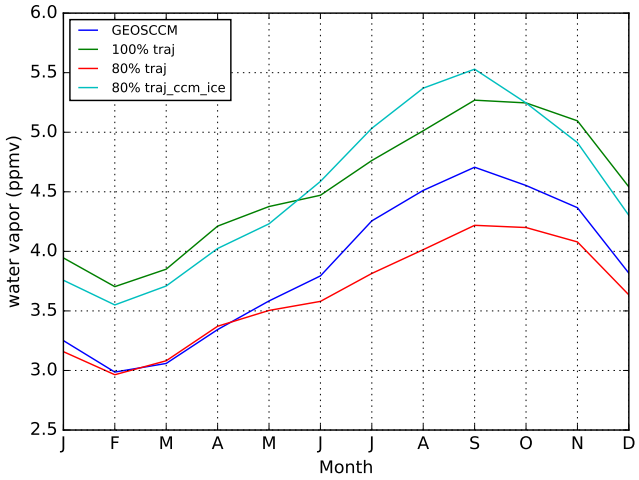

Figure 3.8: Annual cycle of the tropical average water vapor from GEOSCCM simulations (blue) and trajectory model simulations driven by GEOSCCM from 2005 to 2016.

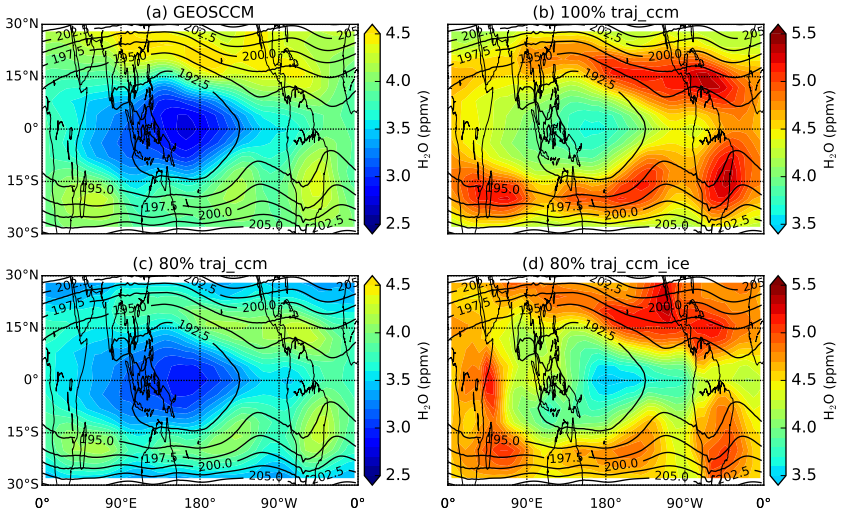

Figure 3.9: Horizontal distribution of TTL water vapor at 100 hPa from 2005 to 2016 from (a) GEOSCCM and (b-d) trajectory model simulations. The contours are the temperature at 100 hPa.

western Pacific Ocean, associated with the coldest TTL temperature (Fig. 3.9). All trajectory model simulations (Figs. 3.9b-d) show similar distributions of TTL water vapor with GEOSCCM simulations, with several centers with high water vapor around 15°S and 15°N. As discussed previously, the magnitude of TTL water vapor from the 80% traj_ccm model is similar to GEOSCCM, while the other two (Figs. 3.9b and 3.9d) show higher values through the tropics. It is noteworthy that the 80% traj_ccm model (Fig. 3.9c) does not simulate the high values over the Asian and North American Monsoons, where the water vapor is obviously increased over same regions after adding evaporation of convective ice (Fig. 3.9d).

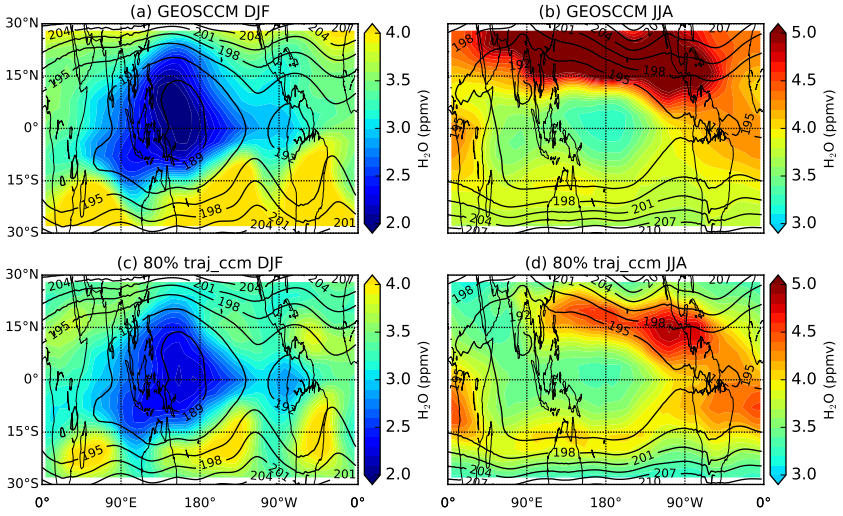

Figure 3.10: Horizontal distribution of TTL water vapor at 100 hPa in (left) DJF and (right) JJA from 2005 to 2016 from (top) GEOSCCM and (bottom) trajectory model simulations. The contours are GEOSCCM temperatures at 100 hPa in (left) DJF and (right) JJA.

We further divide the TTL water vapor into two seasons: DJF and JJA for

GEOSCCM and 80% traj_ccm model. We find that the 80% traj_ccm model agrees well with the GEOSCCM in boreal winter (DJF, Figs. 3.10a and 3.10c), although the detailed structure still has some differences. However, in boreal summer (JJA, Figs. 3.10b and 3.10d), the 80% traj_ccm model obviously fails to simulate the high TTL water vapor over the Northern Hemisphere subtropics, which is the main source of the difference shown in Figs. 3.9a and 3.9c. This disagreement in boreal summer indicates that there might be other sources of TTL water vapor that are not included in the trajectory model, such as evaporation of convective ice from deep convections over monsoon regions in boreal summer.

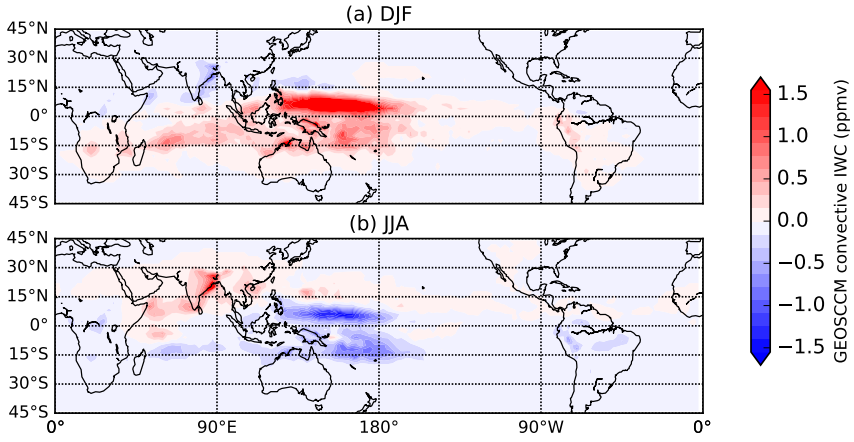

Figure 3.11: Horizontal distribution of convective ice water content (IWC) anomalies at 100 hPa in (a) DJF and (b) JJA from 2005 to 2016 from GEOSCCM. The values have been subtracted from the annual mean IWC.

To seek a possible connection between TTL water vapor and deep convection, we analyze the GEOSCCM's convective cloud IWC at 100 hPa as shown in Fig. 3.11. The horizontal distribution shows positive convective IWC anomalies from

deep convection over monsoon regions in boreal summer (Fig. 3.11b), which matches well with the high TTL water vapor (Fig. 3.10b), indicating that deep convection could moisten the TTL (Corti et al., 2008; Wang and Dessler, 2012; Anderson et al., 2012; Herman et al., 2017; Dessler and Sherwood, 2004; Sun and Huang, 2015; Schwartz et al., 2013). This also explains the high TTL water vapor over Asian and North American monsoon regions after adding evaporation of convective ice in the 80% traj_ccm_ice model (Fig. 3.9d).

Overall, the trajectory model driven by GEOSCCM is capable of accurately reproducing short-term interannual variability of TTL water vapor. The comparison further suggests that the trajectory model should use a saturation threshold around 80%. Some differences still remain — i.e., the trajectory model simulates drier TTL water vapor in summer, especially over Asian and North American monsoon regions. Analysis provides possible evidence of the effect from evaporation of convective ice on the TTL water vapor in summer.

3.2.3 Long-term Water Vapor Simulations

A GEOSCCM run over the whole century allows us to test the capability of the trajectory model to reproduce the GEOSCCM's long-term trend of TTL water vapor. In this section, we will compare the annual average TTL water vapor from trajectory model and GEOSCCM to investigate the mechanism of the increasing trend in TTL water vapor. Substantial portions of this section were published in Dessler et al. (2016).

Fig. 3.12 shows TTL water vapor at 100 hPa during the 21st century. Over the

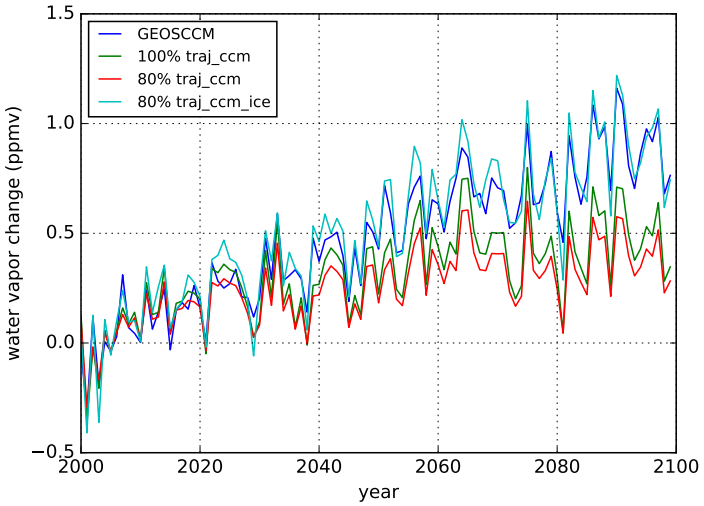

Figure 3.12: Time series of TTL water vapor change at 100 hPa from the GEOSCCM and associated trajectory model runs driven by meteorological fields from GEOSCCM. The water vapor change is calculated by subtracting the average of the first 10 years from each time series. Modified from Figure 1 in Dessler et al. (2016), Copyright (2016) by the American Geophysical Union.

century, the GEOSCCM predicts an increase in tropical average TTL water vapor of 0.9 ppmv between the first and last decade. We simulate TTL water vapor with the trajectory model in the same way as in section 3.2.2, such as "100% traj_ccm" and "80% traj_ccm". We see that the trajectory model predicts smaller increases: TTL water vapor increases by 0.5 ppmv and 0.4 ppmv for the 100% and 80% runs, respectively. Given that the trajectory model is driven by TTL temperatures, we find that much of the increase in water vapor over the 21st century is due to a warming TTL. However, the TTL temperature variations cannot explain all of the TTL water vapor trend.

As discussed in section 3.2.2, the evaporation of convective ice may have some impact on TTL water vapor. We therefore run a trajectory model with a dehydration

threshold of 80%, but adding evaporation of convective ice; we refer to this as the "80% traj_ccm_ice" run (cyan line in Fig. 3.12). After adding evaporation of convective ice, the trajectory model does a better job reproducing the TTL water vapor change over the century, with 0.92 ppmv change from first decade to the last decade, in comparison to 0.9 ppmv from GEOSCCM itself. In other word, the evaporation of convective ice can contribute more than half of the total trend of TTL water vapor in the 21st century.

We do not consider this as opposing to many previous studies that concluded that the TTL temperature variations could entirely explain the observed TTL water vapor variations over the last decade (Fueglistaler et al., 2005, 2009; Randel et al., 2004; Dessler et al., 2014; Wang et al., 2015). Fig. 3.12 also shows that in the first two decades, the convective ice evaporation is just a minor contributor to the TTL water vapor. However, it may play a more important role in long-term trends of TTL and stratospheric water vapor (Dessler et al., 2016).

3.3 Summary

Comparison of TTL water vapor observations to trajectory model simulations show that the trajectory models driven by meteorological fields from reanalyses do a good job in reproducing the basic features of the MLS observations, such as the tape recorder signal, spatial distribution, and tropical average TTL water vapor and anomaly. The agreement indicates that the variability of TTL water vapor during the satellite period is primarily controlled by the TTL temperature. However, the trajectory model simulations still have some quantitative differences, especially

over Asian and North American monsoon regions, suggesting the probability of other sources of TTL water vapor not included in the trajectory model.

We then use what we learned in the comparisons to observations to test a climate model, the GEOSCCM. Comparing a single decade of the model shows that the standard trajectory model is capable of accurately reproducing the GEOSCCM's TTL water vapor. The dry bias from the trajectory model simulated over Asian and North American monsoon regions provides some evidences of the impact of convective ice evaporation on the spatial distribution of TTL water vapor in boreal summer. Analysis of the long-term water vapor change provides solid evidence that the evaporation of convective ice is expected to have a significant contribution to the long-term trend of TTL water vapor in the GEOSCCM over the 21th century.

4. EFFECTS OF CONVECTIVE ICE EVAPORATION ON INTERANNUAL VARIABILITY OF TTL WATER VAPOR*

It is generally recognized that the coldest temperatures in the TTL primarily control the amount of water vapor entering the lower stratosphere (Mote et al., 1996; Holton and Gettelman, 2001). Large interannual variations of TTL water vapor have been observed and attributed to a set of physical processes that affect water vapor by varying TTL temperatures, such as the QBO and BDC. Another important process is deep convection that reaches the TTL and evaporation of convective ice can moisten the TTL (Corti et al., 2008; Wang and Dessler, 2012).

In this section, we will investigate in more detail the physical processes controlling the interannual variations of water vapor in the TTL, particularly the influence of evaporation of convective ice. We use a statistical regression model to decompose the water vapor variability into the dominant physical processes known to drive water vapor. We do this in both observations and water vapor simulated by a trajectory model as discussed in section 3.1. Because the trajectory model does not include convection, differences in the results would be tied to the influence of convection. We verify the methodology by reproducing it in a chemistry-climate model that already includes evaporation of convective ice.

*Reprinted with permission from "Effects of convective ice evaporation on interannual variability of tropical tropopause layer water vapor" by Hao Ye, Andrew E. Dessler, Wandi Yu, 2018, Atmospheric Chemistry and Physics, 18, 4425-4437, Copyright [2018] by Authors.

4.1 Multivariable Linear Regression

To investigate the contributions from different processes to TTL water vapor interannual variations, Dessler et al. (2013, 2014) used a simple linear regression model to fit the observations of tropical average anomalies of 82-hPa water vapor content in the form:

$$\mathrm{H_2O} = a \cdot \mathrm{BDC} + b \cdot \mathrm{QBO} + c \cdot \Delta T + r, \tag{4.1}$$

where BDC, QBO, and ΔT are indices representing the strength of the Brewer-Dobson circulation, the phase of the QBO, and the average tropospheric temperature anomalies of the tropical climate system, respectively. Smalley et al. (2017) verified that this simple approach is also valid in chemistry-climate models.

To gain additional physical insight into the processes associated with TTL water vapor variability, in this paper we perform a similar multivariable regression, but at individual grid points in the TTL:

$$\mathrm{H_2O}(x_i, y_j) = a(x_i, y_j) \cdot \mathrm{BDC} + b(x_i, y_j) \cdot \mathrm{QBO} + c(x_i, y_j) \cdot \Delta T + r(x_i, y_j). \tag{4.2}$$

Here, $\mathrm{H_2O}(x_i, y_j)$ represents the monthly $\mathrm{H_2O}$ anomaly time series at 100 hPa in a grid box centered at longitude x_i and latitude y_j. The coefficients a, b, and c, as well as the residual term r, are also functions of latitude and longitude.

The regressors in Eq. 4.2 are the same tropical average time series used in Dessler et al. (2013, 2014): BDC is a Brewer-Dobson circulation index — here we use the monthly tropical averaged diabatic heating rate anomaly at 82 hPa, with units of $\mathrm{K\,day^{-1}}$. QBO is a quasi-biennial oscillation index and here we use the

standardized monthly zonally averaged equatorial zonal winds anomaly at 50 hPa, with units of $\mathrm{m\,s^{-1}}$. ΔT is the monthly tropical averaged tropospheric temperature anomaly at 500 hPa, with units of degrees K. Because these regressors are tropical average values, they do not vary with location. The QBO index is lagged by 2 months in the regression because the phase of the QBO takes time to impact the TTL temperature and then the water vapor at 100-hPa (Dessler et al., 2013). There is no lag for the BDC and ΔT indices in this study.

4.2 Influence of the BDC and QBO on TTL Water Vapor

We first analyze MLS H_2O observations. We run the regression on these observations twice: Once using BDC and ΔT regressors from the ERAi reanalysis, referred to as "MLS_ERAi", and again using regressors from the MERRA-2 reanalysis, referred to as "MLS_MER2". The QBO index is the same in both regressions and we use monthly index time series downloaded from http://www.cpc.ncep.noaa.gov/data/indices/qbo.u50.index.

The BDC coefficients (Figs. 4.1a and 4.1d) are negative over the tropics, consistent with the idea that an enhanced Brewer-Dobson Circulation cools the TTL (Yulaeva et al., 1994; Randel et al., 2006) and reduces water vapor (Dhomse et al., 2008). The QBO coefficients (Figs. 4.2a and 4.2d) are positive over almost all of the tropics, as the positive phase of QBO tends to decrease the upwelling in TTL, thereby warming it (Plumb and Bell, 1982; Davis et al., 2013).

We also run the regression on H_2O simulated by the trajectory model. We use BDC and ΔT regressors from the same reanalysis used to drive each trajectory

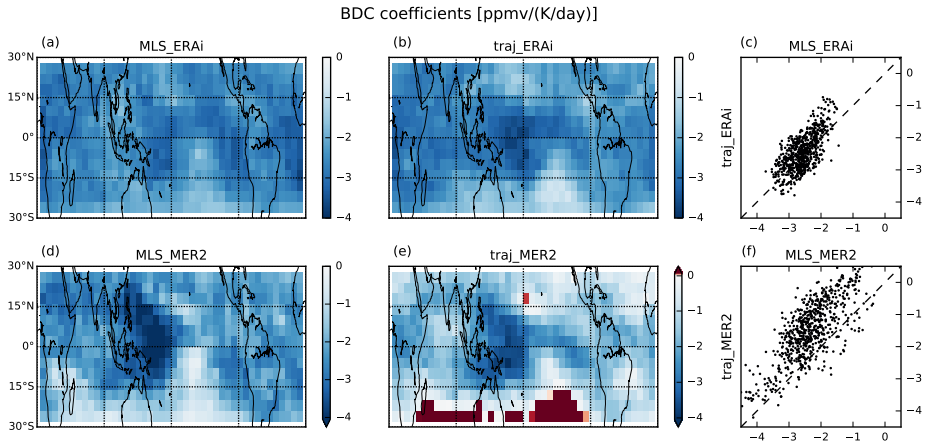

Figure 4.1: (Left column) Multivariate linear regression coefficients of the BDC regressor from MLS H_2O fields, as well as (middle column) the coefficients from regression of the associated trajectory model fields. (Right column) Scatter plots of MLS regressions vs. trajectory model regressions indicate the similarity of the fields. The MLS and associated trajectory regressions cover the period August 2004 to December 2016 between 30°N and 30°S.

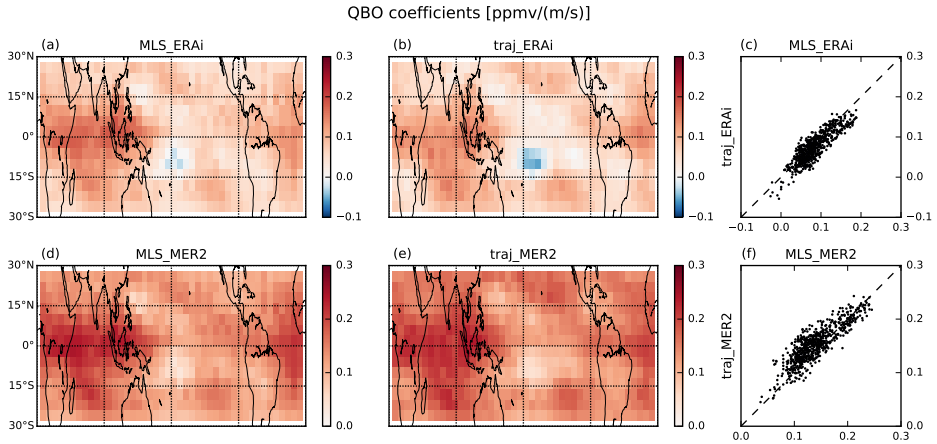

Figure 4.2: Same as Fig. 4.1, but for coefficients of the QBO regressor.

model. First, we use ERAI regressors to analyze the ERAi-driven trajectory model and refer to this as "traj_ERAi". Then, MERRA-2 regressors are used to analyze

the MERRA-2-driven trajectory model and we refer to as "traj_MER2". The QBO index is always obtained from the NCEP observations.

The BDC coefficients from regression of the associated trajectory models (Figs. 4.1b and 4.1e) agree well with the coefficients from the regressions of the MLS observations (Figs. 4.1a and 4.1d). The average BDC coefficient in MLS_ERAi regression (Fig. 4.1a) is -2.6 $\mathrm{ppmv}\,(\mathrm{K\,day^{-1}})^{-1}$, in good agreement with the average value from the accompanying trajectory traj_ERAi regression (Fig. 4.1b), -2.4 $\mathrm{ppmv}\,(\mathrm{K\,day^{-1}})^{-1}$. The gridpoint-by-gridpoint scatter plot (Figs. 2c) demonstrates this agreement in more detail.

The average BDC coefficient in the MLS_MER2 regression (Fig. 4.1d) is -2.3 $\mathrm{ppmv}\,(\mathrm{K\,day^{-1}})^{-1}$. The average coefficient from the accompanying trajectory traj_MER2 regression (Fig. 4.1e) is -1.4 $\mathrm{ppmv}\,(\mathrm{K\,day^{-1}})^{-1}$. This larger difference stems from what appears to be problems in the MERRA-2 heating rates. These heating rates disagree significantly with those from both ERAi as well as the original MERRA. Thus, we put more weight on the ERAi results for this coefficient and conclude that the BDC response is well simulated by the trajectory model.

The QBO coefficients from the regressions of the trajectory models are shown in Figs. 4.2b and 4.2e; gridpoint-by-gridpoint scatter plots are shown in Figs. 4.2c and 4.2f. For the MLS/ERAi comparison (Fig. 4.2c), the average QBO coefficients are 0.084 $\mathrm{ppmv}\,(\mathrm{m\,s^{-1}})^{-1}$ from MLS_ERAi and 0.075 $\mathrm{ppmv}\,(\mathrm{m\,s^{-1}})^{-1}$ from traj_ERAi; for the MLS/MERRA2 comparison (Fig. 4.3f), the average coefficients are 0.14 $\mathrm{ppmv}\,(\mathrm{m\,s^{-1}})^{-1}$ from MLS_MER2 and 0.15 $\mathrm{ppmv}\,(\mathrm{m\,s^{-1}})^{-1}$ from traj_MER2. As with the BDC comparison, the trajectory models do a good job reproducing the regressions of the MLS data.

Overall, we conclude that the trajectory model accurately captures the impact of the BDC and QBO on TTL water vapor — for both the tropical average and the spatial distribution. This supports the hypothesis that these processes mainly influence TTL water vapor by varying large-scale TTL temperatures and transport (Giorgetta and Bengtsson, 1999; Randel et al., 2000; Geller et al., 2002; Randel et al., 2006; Dhomse et al., 2008; Liang et al., 2011; Davis et al., 2013; Dessler et al., 2013, 2014; Wang et al., 2015), which we expect the trajectory model to reproduce. For this reason, we will not focus any further on these coefficients.

4.3 Influence of Tropospheric Temperature on TTL Water Vapor

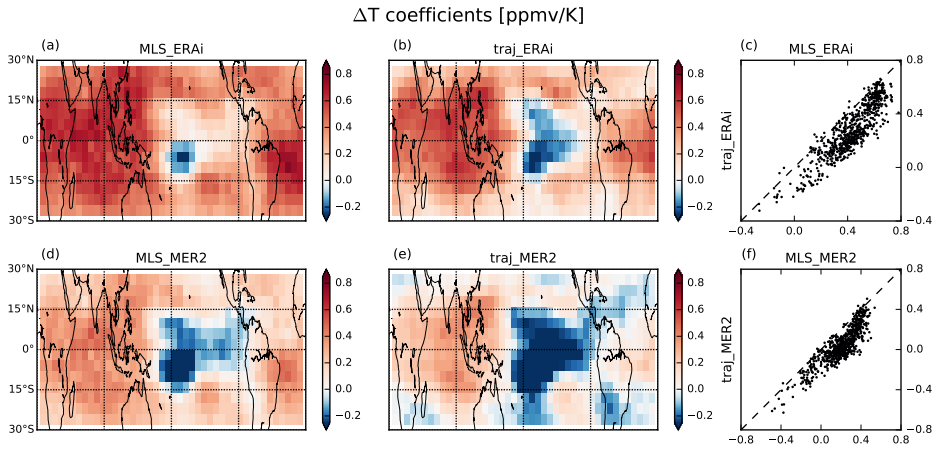

Figure 4.3: Same as Fig. 4.1, but for the coefficient of the ΔT regressor.

Coefficients of ΔT from the MLS regressions are mostly positive, with large

increases over the Tropical Warm Pool region (TWP) and Indian Ocean (Figs. 4.3a and 4.3e), indicating that warming of the tropical troposphere increases the TTL water vapor mixing ratio there. Over the Central Equatorial Pacific (CEP), however, a warming troposphere *decreases* water vapor in the TTL.

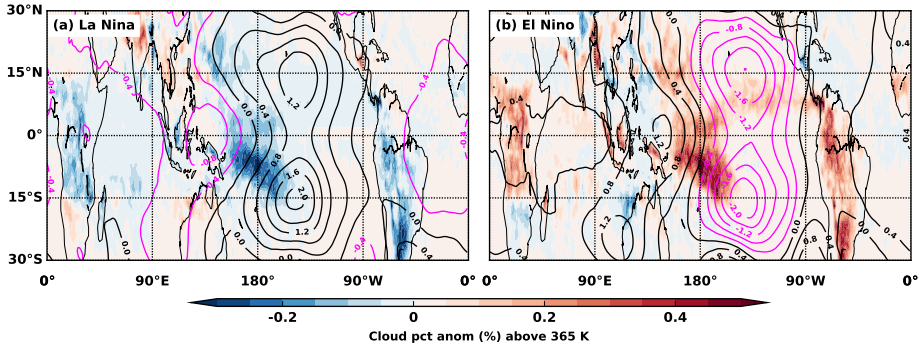

Figure 4.4: Averaged monthly cloud occurrence frequency anomalies above 365 K during (a) La Niña and (b) El Niño months from 2005 to 2016; also shown as contours are temperature anomalies at 100 hPa. La Niña and El Niño months are based on the NOAA Oceanic Niño Index (ONI) in the Niño 3.4 region (5°S to 5°N; 170°W to 120°W).

The decrease in water vapor in the CEP is not entirely unexpected. TTL temperatures are usually coldest — and water vapor a minimum — above the convection maximum in the TWP. As 500-hPa ΔT increases in response to an El Niño event, this convective maximum, and its associated TTL cold pool, shifts eastward from the TWP to the CEP (corresponding to a shift from Figs. 4.4a and 4.4b) (Davis et al., 2013; Hu et al., 2016; Konopka et al., 2016; Avery et al., 2017). Changes in TTL H_2O are expected to mirror this, with increases in water vapor in the TWP and decreases in the CEP as ΔT increases.

Both the MLS and trajectory model regressions show this dipole pattern. However, the MLS regressions yield ΔT coefficients that are systematically higher than those found in the trajectory regressions throughout the tropics (Figs. 4.3c and 4.3f). For the MLS/ERAi comparison (Fig. 4.3c), the average coefficients are 0.43 $\mathrm{ppmv\,K^{-1}}$ from MLS_ERAi and 0.28 $\mathrm{ppmv\,K^{-1}}$ from traj_ERAi; for the MLS/MERRA-2 comparison (Fig. 4.3f), the average coefficients are 0.20 $\mathrm{ppmv\,K^{-1}}$ from MLS_MER2 and 0.05 $\mathrm{ppmv\,K^{-1}}$ from traj_MER2. We have also performed regressions using tropical average values (using Eq. 1, similar to what was done in Dessler et al. (2013, 2014)) and find that the ΔT coefficients from MLS and trajectory models are statistically different with probabilities of 85% and 70% for ERAi and MERRA-2, respectively. This probability is the chance that the two ΔT coefficient probability distributions from MLS and trajectory models are not the same.

We hypothesize that the evaporation of convective ice accounts for the difference between the ΔT coefficients in the MLS and trajectory-model regressions. As convection moves eastward during an El Niño event (Figs. 4.4a and 4.4b), there is an accompanying increase in convective ice in the TTL (Avery et al., 2017), where it evaporates and hydrates the TTL. The moistening from evaporation spreads throughout the tropics and increases the water vapor everywhere. The trajectory model, which does not include either the convection or the convective ice evaporation processes, simulates a smaller increase in water vapor, leading to smaller ΔT coefficients (Figs. 4.3c and 4.3f).

In support of this, in Fig. 4.5 we show that the tropical averaged convective cloud occurrence frequency anomalies at 370 K increase with ΔT. This is consis-

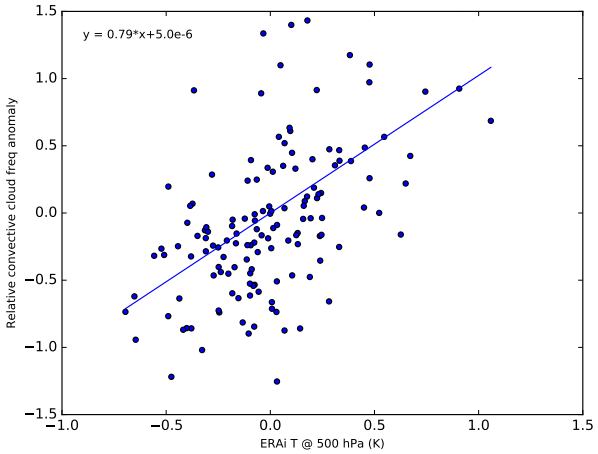

Figure 4.5: Observed convective cloud occurrence frequency anomalies at 390 K and 500-hPa ΔT from ERAi. Values are expressed as the percent change relative to the average cloud frequency at this level (1.2×10^{-6} in tropics). All the data is monthly and tropical averaged from 30°S to 30°N. The straight line is a least-squares fit to the data.

tent with the hypothesis that, as ΔT increases, we should also see an increase in evaporation of cloud ice.

4.4 Tests with a Climate Model

To gain additional confidence in our hypothesis that evaporation of convective ice plays a role in the TTL water budget, we perform a parallel analysis with the GEOSCCM, a model where evaporation of convective ice is known to add water to the TTL (Dessler et al., 2016). To do this, we run a regression on the GEOSCCM 100-hPa H_2O fields as well as on H_2O simulated by a trajectory model driven by the GEOSCCM meteorology, as in section 3.1.

Figs. 4.6a and 4.6b show the spatial distribution of the BDC coefficients from

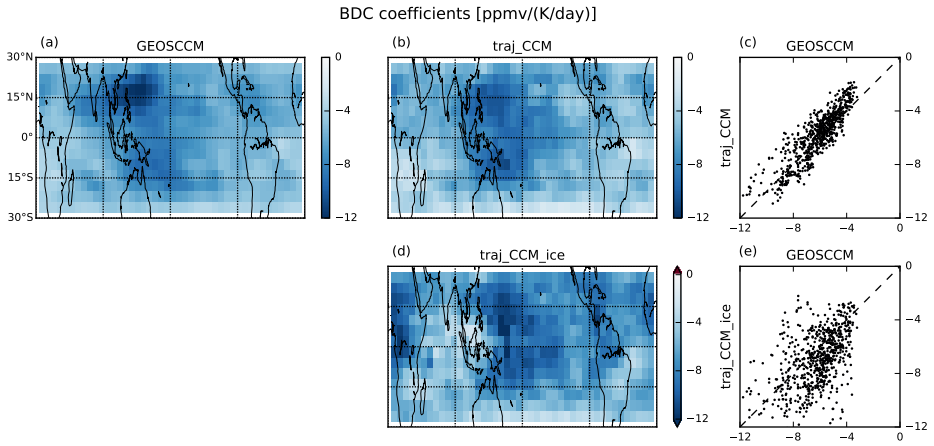

Figure 4.6: (Left column) Multivariate linear regression coefficients of the BDC regressor from GEOSCCM H_2O fields, as well as (middle column) the coefficients from regression of the associated trajectory model fields. (Right column) Scatter plots of GEOSCCM regressions vs. trajectory model regressions indicate the similarity of the fields. The GEOSCCM and associated trajectory run cover 2005-2016 model years between 30°N and 30°S. The bottom row shows coefficients from regressions of a run of the trajectory model driven by GEOSCCM meteorology that includes evaporation of convective ice.

the GEOSCCM and the corresponding trajectory model. This comparison is analogous to the comparison of the regressions on the MLS data and trajectory models driven by reanalyses. The coefficients are similar to each other and to the MLS regressions, suggesting that the GEOSCCM is accurately simulating the impact of BDC changes on TTL water vapor. The influence of the QBO in the version of the GEOSCCM analyzed here does not extend into the TTL, so we have not included a QBO term in the regression and there are consequently no GEOSCCM QBO coefficients.

Before we discuss the ΔT coefficients, it is worth pointing out that the GEOSCCM has realistic ENSO variability in TTL temperatures and convective ice. Figs. 4.7a and 4.7b show that the monthly convective cloud ice water content (IWC) anoma-

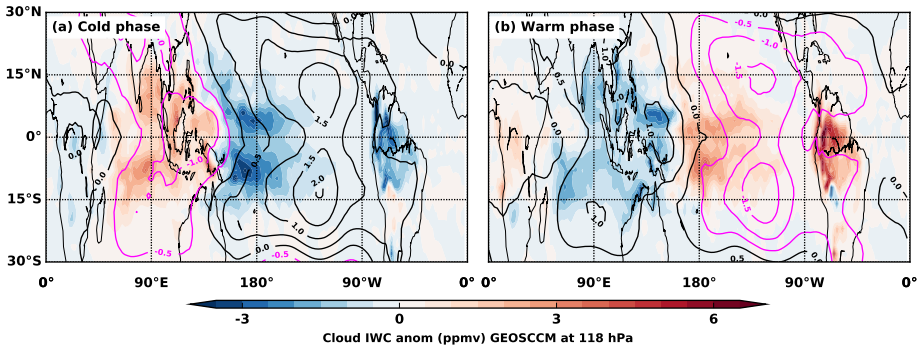

Figure 4.7: Averaged monthly GEOSCCM convective cloud ice water content (IWC) anomalies (ppmv) at 118 hPa during (a) cold and (b) warm GEOSCCM phases from model years 2005 to 2016 with averaged temperature anomalies at 100 hPa shown as contours. The cold and warm phases are defined to be GEOSCCM surface temperature anomaly (departures from the mean annual cycle) of at least -0.5 K and +0.5 K, respectively, in the Niño 3.4 region (same as ONI).

lies at 118 hPa and cold anomalies at 100 hPa in the GEOSCCM shift eastward as ΔT warms from a cold phase (Fig. 4.7a) to a warm phase (Fig. 4.7b), just as they did in observations (Figs. 4.4a and 4.4b).

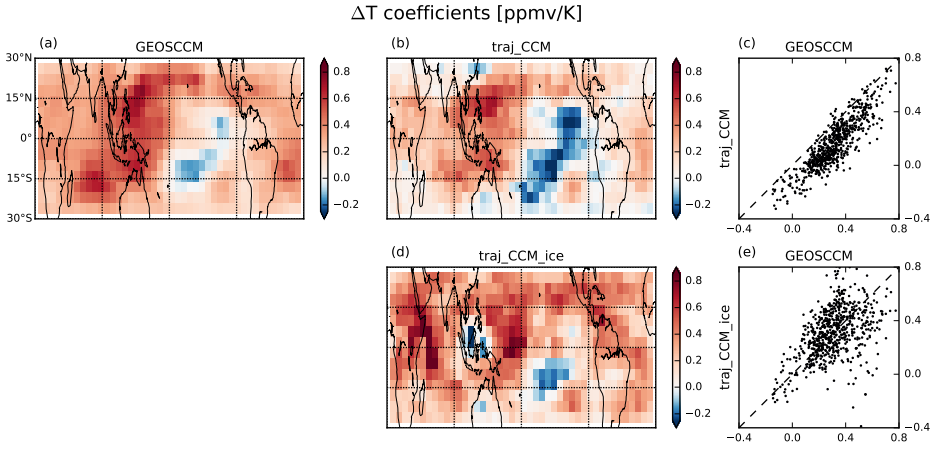

Figure 4.8: Same as Fig. 4.6, but for the coefficient of the ΔT regressor.

The ΔT coefficient fields from the GEOSCCM and associated trajectory regressions (Figs. 4.8a and 4.8b) show the same structural differences as do the ΔT coefficients from the MLS and accompanying trajectory-model regressions — that the ΔT coefficient is larger in the GEOSCCM regression than in the trajectory-model regression; the tropical average ΔT coefficients from GEOSCCM and the trajectory model are significantly different at the 85% confidence level. In the last section, we hypothesized that this difference in the coefficients was due to evaporation of convective ice in the MLS data, a process not included in the trajectory model.

To directly test this hypothesis in the GEOSCCM, we run a second version of the trajectory model that includes the evaporation of convective ice from GEOSCCM, referred to hereafter as traj_ccm_ice. To do this, we use the 6-hourly three-dimensional convective cloud IWC field from GEOSCCM and linearly interpolate it to each parcel's position at every time step. We then assume instantaneous and complete evaporation of this ice into the parcel by adding the IWC to the parcel's water vapor, although we do not let parcels exceed 100% relative humidity with respect to ice. This is the same procedure used to simulate convective ice evaporation by Dessler et al. (2016) .

We then run the regression on the traj_ccm_ice's H_2O field. The scatter plot of GEOSCCM vs. traj_ccm_ice BDC coefficients (Fig. 4.6e) shows larger scatter than the comparison without ice (Fig. 4.6c). The increase in scatter is likely the result of the crudeness of our microphysical assumptions, particularly the assumption that convective ice evaporates instantaneously. However, the comparison between the tropical average GEOSCCM BDC coefficient, -6.2 $\mathrm{ppmv}\,(\mathrm{K\,day^{-1}})^{-1}$ (Fig. 4.6a),

and those from the trajectory models, -5.8 (Fig. 4.6b) and -6.9 $\mathrm{ppmv}\,(\mathrm{K\,day^{-1}})^{-1}$ (Fig. 4.6d) without and with convective ice evaporation, respectively, is similar.

The scatter plot of GEOSCCM vs. traj_ccm_ice ΔT coefficients (Fig. 4.8e) similarly shows larger scatter than the comparison without ice (Fig. 4.8c). Adding ice does, however, increase the average ΔT coefficient (seen by comparing Figs 4.8c to 4.8e), from 0.16 $\mathrm{ppmv\,K^{-1}}$ to 0.32 $\mathrm{ppmv\,K^{-1}}$, bringing the trajectory model into closer agreement with the GEOSCCM, which has a corresponding value of 0.31 $\mathrm{ppmv\,K^{-1}}$. There are also some interesting changes in the spatial pattern of the traj_ccm_ice (Fig. 4.8d). For example, negative ΔT coefficients appear in the TWP and Indonesia in the traj_ccm_ice regression. The cause of this is unknown, but also is likely linked to the trajectory model's ice evaporation assumption.

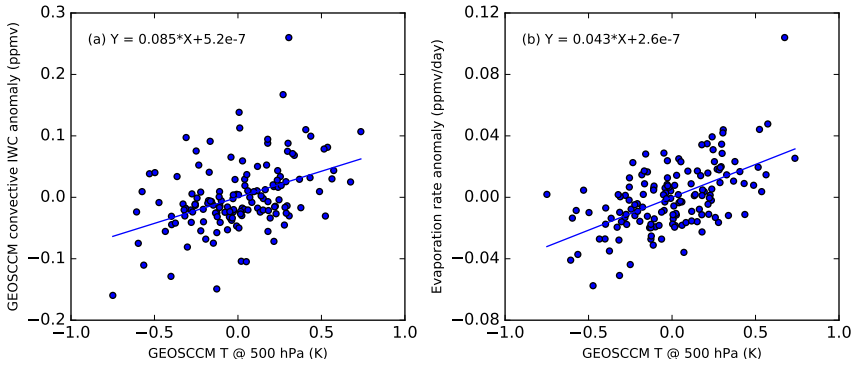

Figure 4.9: (a) Convective IWC anomalies at 100 hPa and ΔT from GEOSCCM. (b) GEOSCCM convective cloud evaporation rate anomalies at 100 hPa and ΔT. All the data is monthly and tropical averaged from 30°S to 30°N. The straight lines are least-squares fits to the data.

We showed in the previous section that the observed convective cloud occurrence frequency in the TTL increased as ΔT increased (Fig. 4.5) and we also see

that the GEOSCCM simulates a similar correlation between convective cloud IWC and ΔT (Fig. 4.9a). While these are not exactly the same quantity, they show a consistency that provides confidence that the behavior of the model is realistic.

Finally, to quantify convective ice evaporation, we calculate the evaporation rate of convective ice at 100 hPa in the trajectory model. To do this, we save the amount of water added to each parcel by ice evaporation in every time step. We then bin and average the amount evaporated to come up with the distribution of the amount evaporated per day. Note that much of this water added will be lost in subsequent dehydration events, so this does not represent net water added to the stratosphere.

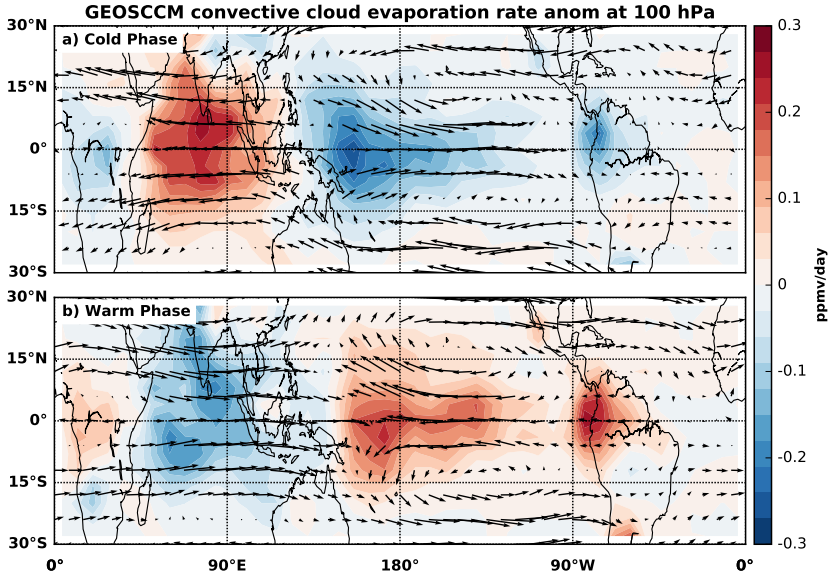

Figure 4.10: Averaged monthly GEOSCCM convective cloud evaporation rate anomalies at 100 hPa during (a) cold and (b) warm GEOSCCM phases from 2005 to 2016. Also shown are averaged horizontal wind anomaly vectors at 100 hPa.

Fig. 4.9b shows that the tropical average evaporation rate of convective ice also increases with ΔT, which provides further evidence that the difference in ΔT coefficients between the GEOSCCM and the trajectory model is due to evaporation of convective ice. Fig. 4.10 shows the distribution of monthly averaged evaporation rate during ENSO-like warm and cold phases in the GEOSCCM. We see that, as ΔT increases and we transition from a cold to warm phase of variability, the location of ice evaporation shifts from the TWP and Indian Ocean to the CEP. This is consistent with the analysis of Avery et al. (2017).

4.5 Summary

Previous work has shown that TTL water vapor variability is mainly controlled by TTL temperature variability (Mote et al., 1996; Holton and Gettelman, 2001; Fueglistaler et al., 2009). In particular, variations in the Brewer-Dobson circulation (BDC) and the quasi-biennial oscillation (QBO) play key roles (Fueglistaler and Haynes, 2005; Geller et al., 2002; Liang et al., 2011; Liess and Geller, 2012; Calvo et al., 2010; Randel et al., 2006; Dessler et al., 2013, 2014; Tao et al., 2015). It has been suggested by many previous investigators that evaporation of convective ice may also contribute water to the TTL (Khaykin et al., 2009; Hassim and Lane, 2010; Carminati et al., 2014; Frey et al., 2015; Virts and Houze, 2015; Schoeberl and Dessler, 2011; Schoeberl et al., 2014; Ueyama et al., 2014, 2015; Dessler et al., 2016; Avery et al., 2017). In this paper, we analyze the spatial distribution of TTL water vapor and conclude that, indeed, convection makes a small contribution to the interannual variability over the MLS period.

To do that, we use a linear regression model on TTL water vapor at individual grid points over the tropics to investigate the spatial distribution of the impact of the BDC, QBO, and tropospheric temperature (ΔT). We run this linear regression model on MLS observations of TTL water vapor anomalies and on water vapor anomalies simulated by a trajectory model that only includes the effects of TTL temperatures on water vapor.

The spatial patterns and magnitudes of the BDC and QBO coefficients agree well between MLS observations and associated trajectory model simulations. This suggests that, consistent with expectations, these processes affect TTL water vapor mainly by changing TTL temperatures (Randel et al., 2000; Geller et al., 2002; Randel et al., 2006; Dhomse et al., 2008; Liang et al., 2011; Davis et al., 2013; Dessler et al., 2013, 2014).

The spatial distribution of ΔT coefficients has an obvious dipole structure associated with the ENSO (Konopka et al., 2016): Negative values in the CEP, where temperatures decrease as the troposphere warms, and positive values in the TWP, where the opposite occurs.

We also find that ΔT coefficients from the MLS observations are larger throughout the tropics than in the trajectory model. We hypothesize that changes in convection as ΔT increases leads to increases in evaporation of convective ice in the TTL. This increases the ΔT coefficient in the MLS analysis, but not in the trajectory model, which does not have convective ice evaporation in it. We see support for this in the observations of increased convective cloud occurrence frequency in the TTL as ΔT increases. This result is also in agreement with the case study in Avery et al. (2017) as well as the model analysis in Schoeberl and Dessler (2011),

Schoeberl et al. (2014), and Ueyama et al. (2014, 2015).

To gain additional confidence in our hypothesis that evaporation of convective ice is responsible for the difference in ΔT coefficients, we test the methodology in a parallel analysis with the GEOSCCM, a model where evaporation of convective ice is known to add water to the TTL (Dessler et al., 2016). We find that the results of this analysis show the same difference — that the ΔT coefficients from the regression of the GEOSCCM's water vapor field are larger than the coefficients from a trajectory model driven by GEOSCCM meteorology.

We confirm this is due to evaporation of convective ice by running a second version of the trajectory model, which includes convective ice evaporation. We find that the ΔT coefficient from the regression of this version of the trajectory model is in agreement with that from the GEOSCCM regression.

Putting all of these together, we conclude that variability in the evaporation of convective ice plays a role in water vapor variability in the TTL. Our work should not be taken as opposing previous research (Randel et al., 2006; Schiller et al., 2009; Wright et al., 2011; Randel and Jensen, 2013) that concluded most of the variance in TTL water vapor over the last few decades is due to TTL temperatures. We concur that the impact of convective ice only is a minor contributor to TTL water vapor variability over the period spanned by the MLS data. But for GEOSCCM, which does an excellent job simulating TTL water vapor over the comparable period, suggests that convective ice may play a much larger role in future long-term trends of TTL and stratospheric water vapor (Dessler et al., 2016), so more research on this phenomenon is clearly warranted.

5. CONCLUSIONS AND FUTURE DIRECTIONS

5.1 Conclusions

Water vapor in the TTL has a significant impact on the global energy budget and contributes to a possibly significant stratospheric water vapor feedback (Dessler et al., 2013). The amount of TTL water vapor is primarily controlled by TTL temperature. But convection can also influence the TTL, although its contribution to TTL variability remains uncertain. In this dissertation, we focus on understanding what physical processes control the spatial distribution of TTL water vapor and the impact of deep convection on TTL water vapor.

Our main tool is a Lagrangian trajectory model with large-scale circulation and temperature fields. It has previously demonstrated the capability to accurately reproduce TTL water vapor. Most of our analyses are comparison of TTL water vapor simulations from the trajectory model to satellite observations and climate model simulations.

The results of this dissertation are divided into two main parts in chapters 3 and 4. The first part (chapter 3) investigates the capability of the trajectory model to simulate the basic properties of the TTL water vapor in the satellite observations and climate model simulations. By comparing to MLS observations, we found that the trajectory model driven by meteorological fields from reanalyses does an excellent job of reproducing the basic features of TTL water vapor. This good agreement indicates that, over the satellite period, TTL water vapor variations are primarily controlled by variability of the TTL temperature, in agreement with previ-

ous research. However, the quantitative differences in TTL water vapor over Asian and North American Monsoon regions indicate that the trajectory model is missing some potentially important sources of water vapor.

We also compare TTL water vapor from the trajectory model to climate model simulations. Over short periods (e.g., one decade), the trajectory model accurately reproduces the interannual variations of TTL water vapor in the climate model. However, quantitative differences similar to those seen in the satellite data also exist between the trajectory model and the climate model. We further find that the differences seem associated with the distribution of GEOSCCM convective cloud IWC, providing possible evidence of the effect from evaporation of convective ice on the TTL water vapor.

On longer timescales (i.e., over the 21st century), the TTL water vapor from the trajectory model shows clear differences from the GEOSCCM. However, if we add convective ice evaporation to the trajectory model, we obtain good agreement with the GEOSCCM simulation. Therefore, the evaporation of convective ice plays an important role and contributes to more than half of the total trend of TTL water vapor in the 21st century.

The second part (chapter 4) investigates the physical processes associated with the spatial distribution of TTL water vapor variability. Using a multivariate linear regression model to decompose TTL water vapor variability, we investigate the impact of the BDC, QBO, and tropospheric temperature (ΔT) on the spatial distribution of TTL water vapor. The good agreement in the spatial pattern and magnitude of BDC and QBO coefficients between trajectory model simulations and MLS observations indicates that the BDC and QBO affect TTL water vapor mainly by

changing TTL temperatures.

The spatial pattern of the ΔT coefficients shows a dipole structure in both the trajectory model and MLS observations, which is associated with ENSO. However, we also find that MLS observations have larger ΔT coefficient values throughout the tropics than trajectory model simulations. We hypothesize that this difference is due to increases in convective ice evaporation in the TTL as ΔT increases, a process not included in the trajectory model. This is supported by the increases in convective cloud occurrence frequency.

We test our methodology by performing a parallel analysis in the GEOSCCM, which has known ice evaporation. This shows similar larger ΔT coefficients in the regression of the GEOSCCM's water vapor, compared to a trajectory model driven by GEOSCCM meteorology. After adding convective ice evaporation into the trajectory model, we find better agreement between the ΔT coefficients from the trajectory model and the GEOSCCM regressions. This provides some confidence that variability in the evaporation of convective ice plays a role in water vapor variability in the TTL.

Putting these two parts together, we concur that the impact of convective ice evaporation is a minor contributor to TTL water vapor variability over the short period spanned by the MLS data. But on longer time scales, convective ice evaporation may play a much larger role in long-term trends of TTL and stratospheric water vapor.

5.2 Future Directions

Many aspects of the TTL water vapor are yet to be fully understood in both satellite observations and model simulations. Important unsolved problems include:

1. Although our trajectory model is able to reproduce TTL water vapor interannual variability well, many aspects of the trajectory model could be improved, such as the simple consideration of saturation threshold and the assumption of instant removal of frozen ice from dehydration. Trajectory models combined with a cloud model can simulate more complex physics and are sometimes able to obtain more accurate TTL water vapor (e.g. Schoeberl et al., 2014; Ueyama et al., 2015).

2. As mentioned in section 3.1.3, the trajectory model fails to reproduce the high TTL water vapor over Asian and North American Monsoon regions in boreal summer. This is likely due to the lack of deep convection over corresponding regions in boreal summer in the model. Quantitative investigation in these regions with a trajectory model could improve the understanding of how these regions influence TTL and stratospheric water vapor.

REFERENCES

Anderson, J. G., Wilmouth, D. M., Smith, J. B., and Sayres, D. S.: UV dosage levels in summer: Increased risk of ozone loss from convectively injected water vapor, Science, 337, 835–839, https://doi.org/10.1126/science.1222978, 2012.

Avery, M. A., Davis, S. M., Rosenlof, K. H., Ye, H., and Dessler, A. E.: Large anomalies in lower stratospheric water vapour and ice during the 2015-2016 El Niño, Nat. Geosci., 10, 405–409, https://doi.org/10.1038/NGEO2961, 2017.

Bacmeister, J. T., Suarez, M. J., and Robertson, F. R.: Rain reevaporation, boundary layer–convection interactions, and Pacific rainfall patterns in an AGCM, J. Atmos. Sci., 63, 3383–3403, https://doi.org/10.1175/JAS3791.1, 2006.

Barahona, D., Molod, A., Bacmeister, J., Nenes, A., Gettelman, A., Morrison, H., Phillips, V., and Eichmann, A.: Development of two-moment cloud microphysics for liquid and ice within the NASA Goddard Earth Observing System Model (GEOS-5), Geosci. Model Dev., 7, 1733–1766, https://doi.org/10.5194/gmd-7-1733-2014, 2014.

Bergman, J. W., Jensen, E. J., Pfister, L., and Yang, Q.: Seasonal differences of vertical-transport efficiency in the tropical tropopause layer: On the interplay between tropical deep convection, large-scale vertical ascent, and horizontal circulations, J. Geophys. Res.-Atmos., 117, https://doi.org/10.1029/2011JD016992, 2012.

Bernath, P. F., McElroy, C. T., Abrams, M. C., Boone, C. D., Butler, M., CamyâĂŘPeyret, C., Carleer, M., Clerbaux, C., Coheur, P., Colin, R., DeCola, P., DeMazière, M., Drummond, J. R., Dufour, D., Evans, W. F. J., Fast, H., Fussen,

D., Gilbert, K., Jennings, D. E., Llewellyn, E. J., Lowe, R. P., Mahieu, E., McConnell, J. C., McHugh, M., McLeod, S. D., Michaud, R., Midwinter, C., Nassar, R., Nichitiu, F., Nowlan, C., Rinsland, C. P., Rochon, Y. J., Rowlands, N., Semeniuk, K., Simon, P., Skelton, R., Sloan, J. J., Soucy, M., Strong, K., Tremblay, P., Turnbull, D., Walker, K. A., Walkty, I., Wardle, D. A., Wehrle, V., Zander, R., and Zou, J.: Atmospheric chemistry experiment (ACE): Mission overview, Geophys. Res. Lett., 32, https://doi.org/10.1029/2005GL022386, 2005.

Bosilovich, M., Lucchesi, R., and Suarez, M.: MERRA-2: File specification, GMAO Office Note No. 9 (Version 1.1), Tech. Rep. Version 1.1, Global Modeling and Assimilation Office, 2016.

Bowman, K. P.: Large-scale isentropic mixing properties of the Antarctic polar vortex from analyzed winds, J. Geophys. Res.-Atmos., 98, 23 013–23 027, https://doi.org/10.1029/93JD02599, 1993.

Bowman, K. P. and Carrie, G. D.: The mean-meridional transport circulation of the troposphere in an idealized GCM, J. Atmos. Sci., 59, 1502–1514, https://doi.org/10.1175/1520-0469(2002)059<1502:TMMTCO>2.0.CO;2, 2002.

Brewer, A.: Evidence for a world circulation provided by the measurements of helium and water vapour distribution in the stratosphere, Q. J. Royal Meteorol. Soc., 75, 351–363, https://doi.org/10.1002/qj.49707532603, 1949.

Calvo, N., Garcia, R., Randel, W., and Marsh, D.: Dynamical mechanism for the increase in tropical upwelling in the lowermost tropical stratosphere during warm ENSO events, J. Atmos. Sci., 67, 2331–2340, https://doi.org/10.1175/2010JAS3433.1, 2010.

Carminati, F., Ricaud, P., Pommereau, J.-P., Rivière, E., Khaykin, S., Attié, J.-

L., and Warner, J.: Impact of tropical land convection on the water vapour budget in the tropical tropopause layer, Atmos. Chem. Phys., 14, 6195–6211, https://doi.org/10.5194/acp-14-6195-2014, 2014.

Chu, W., McCormick, M., Lenoble, J., Brogniez, C., and Pruvost, P.: SAGE II inversion algorithm, J. Geophys. Res.-Atmos., 94, 8339–8351, https://doi.org/10.1029/JD094iD06p08339, 1989.

Corti, T., Luo, B., De Reus, M., Brunner, D., Cairo, F., Mahoney, M., Martucci, G., Matthey, R., Mitev, V., Dos Santos, F., Schiller, C., Shur, G., Sitnikov, N., Spelten, N., Vössing, H., Borrmann, S., and Peter, T.: Unprecedented evidence for deep convection hydrating the tropical stratosphere, Geophys. Res. Lett., 35, https://doi.org/10.1029/2008GL033641, 2008.

Davis, S. M., Liang, C. K., and Rosenlof, K. H.: Interannual variability of tropical tropopause layer clouds, Geophys. Res. Lett., 40, 2862–2866, https://doi.org/10.1002/grl.50512, 2013.

Dee, D. P., Uppala, S. M., Simmons, A. J., Berrisford, P., Poli, P., Kobayashi, S., Andrae, U., Balmaseda, M. A., Balsamo, G., Bauer, P., Bechtold, P., Beljaars, A. C. M., van de Berg, L., Bidlot, J., Bormann, N., Delsol, C., Dragani, R., Fuentes, M., Geer, A. J., Haimberger, L., Healy, S. B., Hersbach, H., Hólm, E. V., Isaksen, L., Kållberg, P., Köhler, M., Matricardi, M., McNally, A. P., MongeâĂŘSanz, B. M., Morcrette, J., Park, B., Peubey, C., de Rosnay, P., Tavolato, C., Thépaut, J., and Vitart, F.: The ERA-Interim reanalysis: Configuration and performance of the data assimilation system, Q. J. Royal Meteorol. Soc., 137, 553–597, https://doi.org/10.1002/qj.828, 2011.

Dessler, A. and Sherwood, S.: Effect of convection on the summertime extratropical

lower stratosphere, J. Geophys. Res.-Atmos., 109, D23 301, https://doi.org/10.1029/2004JD005209, 2004.

Dessler, A., Hanisco, T., and Fueglistaler, S.: Effects of convective ice lofting on H_2O and HDO in the tropical tropopause layer, J. Geophys. Res.-Atmos., 112, https://doi.org/10.1029/2007JD008609, 2007.

Dessler, A., Schoeberl, M., Wang, T., Davis, S., and Rosenlof, K.: Stratospheric water vapor feedback, P. Natl. Acad. Sci. USA, 110, 18 087–18 091, https://doi.org/10.1073/pnas.1310344110, 2013.

Dessler, A., Schoeberl, M., Wang, T., Davis, S., Rosenlof, K., and Vernier, J.-P.: Variations of stratospheric water vapor over the past three decades, J. Geophys. Res.-Atmos., 119, https://doi.org/10.1002/2014JD021712, 2014.

Dessler, A., Ye, H., Wang, T., Schoeberl, M., Oman, L., Douglass, A., Butler, A., Rosenlof, K., Davis, S., and Portmann, R.: Transport of ice into the stratosphere and the humidification of the stratosphere over the 21st century, Geophys. Res. Lett., 43, 2323–2329, https://doi.org/10.1002/2016GL067991, 2016.

Dhomse, S., Weber, M., and Burrows, J.: The relationship between tropospheric wave forcing and tropical lower stratospheric water vapor, Atmos. Chem. Phys., 8, 471–480, https://doi.org/10.5194/acp-8-471-2008, 2008.

Dobson, G.: Origin and distribution of the polyatomic molecules in the atmosphere, Proc. Royal Soc. A, 236, 187–193, https://doi.org/10.1098/rspa.1956.0127, 1956.

Frey, W., Schofield, R., Hoor, P., Kunkel, D., Ravegnani, F., Ulanovsky, A., Viciani, S., D'amato, F., and Lane, T.: The impact of overshooting deep convection on local transport and mixing in the tropical upper troposphere/lower stratosphere (UTLS), Atmos. Chem. Phys., 15, 6467–6486, https://doi.org/10.5194/

acp-15-6467-2015, 2015.

Fueglistaler, S. and Haynes, P.: Control of interannual and longer-term variability of stratospheric water vapor, J. Geophys. Res.-Atmos., 110, https://doi.org/10.1029/2005JD006019, 2005.

Fueglistaler, S., Bonazzola, M., Haynes, P., and Peter, T.: Stratospheric water vapor predicted from the Lagrangian temperature history of air entering the stratosphere in the tropics, J. Geophys. Res.-Atmos., 110, https://doi.org/10.1029/2004JD005516, 2005.

Fueglistaler, S., Dessler, A., Dunkerton, T., Folkins, I., Fu, Q., and Mote, P. W.: Tropical tropopause layer, Rev. Geophys., 47, https://doi.org/10.1029/2008RG000267, 2009.

Garfinkel, C., Waugh, D., Oman, L., Wang, L., and Hurwitz, M.: Temperature trends in the tropical upper troposphere and lower stratosphere: Connections with sea surface temperatures and implications for water vapor and ozone, J. Geophys. Res.-Atmos., 118, 9658–9672, https://doi.org/10.1002/jgrd.50772, 2013.

Geller, M. A., Zhou, X., and Zhang, M.: Simulations of the interannual variability of stratospheric water vapor, J. Atmos. Sci., 59, 1076–1085, https://doi.org/10.1175/1520-0469(2002)059<1076:SOTIVO>2.0.CO;2, 2002.

Gettelman, A., Randel, W., Massie, S., Wu, F., Read, W. G., and Russell III, J.: El Niño as a natural experiment for studying the tropical tropopause region, J. Clim., 14, 3375–3392, https://doi.org/10.1175/1520-0442(2001)014<3375:ENOAAN>2.0.CO;2, 2001.

Gettelman, A., Birner, T., Eyring, V., Akiyoshi, H., Bekki, S., Brühl, C., Dameris, M., Kinnison, D. E., Lefevre, F., Lott, F., Mancini, E., Pitari, G., Plummer, D. A.,

Rozanov, E., Shibata, K., Stenke, A., Struthers, H., and Tian, W.: The tropical tropopause layer 1960–2100, Atmos. Chem. Phys., 9, 1621–1637, https://doi.org/10.5194/acp-9-1621-2009, 2009.

Gettelman, A., Hegglin, M. I., Son, S., Kim, J., Fujiwara, M., Birner, T., Kremser, S., Rex, M., AÃśel, J. A., Akiyoshi, H., Austin, J., Bekki, S., Braesike, P., BrÃijhl, C., Butchart, N., Chipperfield, M., Dameris, M., Dhomse, S., Garny, H., Hardiman, S. C., JÃűckel, P., Kinnison, D. E., Lamarque, J. F., Mancini, E., Marchand, M., Michou, M., Morgenstern, O., Pawson, S., Pitari, G., Plummer, D., Pyle, J. A., Rozanov, E., Scinocca, J., Shepherd, T. G., Shibata, K., Smale, D., TeyssÃĺdre, H., and Tian, W.: Multimodel assessment of the upper troposphere and lower stratosphere: Tropics and global trends, J. Geophys. Res.-Atmos., 115, https://doi.org/10.1029/2009JD013638, 2010.

Giorgetta, M. A. and Bengtsson, L.: Potential role of the quasi-biennial oscillation in the stratosphere-troposphere exchange as found in water vapor in general circulation model experiments, J. Geophys. Res.-Atmos., 104, 6003–6019, https://doi.org/10.1029/1998JD200112, 1999.

Hassim, M. and Lane, T.: A model study on the influence of overshooting convection on TTL water vapour, Atmos. Chem. Phys., 10, 9833–9849, https://doi.org/10.5194/acp-10-9833-2010, 2010.

Haynes, P. and Shuckburgh, E.: Effective diffusivity as a diagnostic of atmospheric transport: 2. Troposphere and lower stratosphere, J. Geophys. Res.-Atmos., 105, 22 795–22 810, https://doi.org/10.1029/2000JD900092, 2000.

Held, I. M. and Soden, B. J.: Water vapor feedback and global warming, Annu. Rev. Environ. Resour., 25, 441–475, https://doi.org/10.1146/annurev.energy.25.1.441,

2000.

Herman, R. L., Ray, E. A., Rosenlof, K. H., Bedka, K. M., Schwartz, M. J., Read, W. G., Troy, R. F., Chin, K., Christensen, L. E., Fu, D., Stachnik, R. A., Bui, T. P., and Dean-Day, J. M.: Enhanced stratospheric water vapor over the summertime continental United States and the role of overshooting convection, Atmos. Chem. Phys., 17, 6113, https://doi.org/10.5194/acp-17-6113-2017, 2017.

Highwood, E. and Hoskins, B.: The tropical tropopause, Q. J. Royal Meteorol. Soc., 124, 1579–1604, https://doi.org/10.1256/smsqj.54910, 1998.

Holton, J. R. and Gettelman, A.: Horizontal transport and the dehydration of the stratosphere, Geophys. Res. Lett., 28, 2799–2802, https://doi.org/10.1029/2001GL013148, 2001.

Holton, J. R., Haynes, P. H., McIntyre, M. E., Douglass, A. R., Rood, R. B., and Pfister, L.: Stratosphere-troposphere exchange, Rev. Geophys., 33, 403–439, https://doi.org/10.1029/95RG02097, 1995.

Hoskins, B. J.: Towards a PV-θ view of the general circulation, Tellus A, 43, 27–36, https://doi.org/10.1034/j.1600-0889.1991.t01-3-00005.x, 1991.

Hoskins, B. J., McIntyre, M., and Robertson, A. W.: On the use and significance of isentropic potential vorticity maps, Q. J. Royal Meteorol. Soc., 111, 877–946, https://doi.org/10.1256/smsqj.47001, 1985.

Hu, D., Tian, W., Guan, Z., Guo, Y., and Dhomse, S.: Longitudinal asymmetric trends of tropical cold-point tropopause temperature and their link to strengthened Walker circulation, J. Clim., 29, 7755–7771, https://doi.org/10.1175/JCLI-D-15-0851.1, 2016.

Jiang, J. H., Su, H., Zhai, C., Wu, L., Minschwaner, K., Molod, A. M., and Tomp-

kins, A. M.: An assessment of upper troposphere and lower stratosphere water vapor in MERRA, MERRA2, and ECMWF reanalyses using Aura MLS observations, J. Geophys. Res.-Atmos., 120, https://doi.org/10.1002/2015JD023752, 2015.

Khaykin, S., Pommereau, J.-P., Korshunov, L., Yushkov, V., Nielsen, J., Larsen, N., Christensen, T., Garnier, A., Lukyanov, A., and Williams, E.: Hydration of the lower stratosphere by ice crystal geysers over land convective systems, Atmos. Chem. Phys., 9, 2275–2287, https://doi.org/10.5194/acp-9-2275-2009, 2009.

Kim, J., Grise, K. M., and Son, S.-W.: Thermal characteristics of the cold-point tropopause region in CMIP5 models, J. Geophys. Res.-Atmos., 118, 8827–8841, https://doi.org/10.1002/jgrd.50649, 2013.

Kirk-Davidoff, D. B., Hintsa, E. J., Anderson, J. G., and Keith, D. W.: The effect of climate change on ozone depletion through changes in stratospheric water vapour, Nature, 402, 399, https://doi.org/10.1038/46521, 1999.

Kley, D., Stone, E., Henderson, W., Drummond, J., Harrop, W., Schmeltekopf, A., Thompson, T., and Winkler, R.: In situ measurements of the mixing ratio of water vapor in the stratosphere, J. Atmos. Sci., 36, 2513–2524, https://doi.org/10.1175/1520-0469(1979)036<2513:SMOTMR>2.0.CO;2, 1979.

Konopka, P., Ploeger, F., Tao, M., and Riese, M.: Zonally resolved impact of ENSO on the stratospheric circulation and water vapor entry values, J. Geophys. Res.-Atmos., 121, https://doi.org/10.1002/2015JD024698, 2016.

Lambert, A., Read, W. G., Livesey, N. J., Santee, M. L., Manney, G. L., Froidevaux, L., Wu, D. L., Schwartz, M. J., Pumphrey, H. C., Jimenez, C., Nedoluha, G. E., Cofield, R. E., Cuddy, D. T., Daffer, W. H., Drouin, B. J., Fuller, R. A.,

Jarnot, R. F., Knosp, B. W., Pickett, H. M., Perun, V. S., Snyder, W. V., Stek, P. C., Thurstans, R. P., Wagner, P. A., Waters, J. W., Jucks, K. W., Toon, G. C., Stachnik, R. A., Bernath, P. F., Boone, C. D., Walker, K. A., Urban, J., Murtagh, D., Elkins, J. W., and Atlas, E.: Validation of the Aura Microwave Limb Sounder middle atmosphere water vapor and nitrous oxide measurements, J. Geophys. Res.-Atmos., 112, D24S36, https://doi.org/10.1029/2007JD008724, 2007.

Lee, J., Yang, P., Dessler, A. E., Gao, B.-C., and Platnick, S.: Distribution and radiative forcing of tropical thin cirrus clouds, J. Atmos. Sci., 66, 3721–3731, https://doi.org/10.1175/2009JAS3183.1, 2009.

Liang, C., Eldering, A., Gettelman, A., Tian, B., Wong, S., Fetzer, E., and Liou, K.: Record of tropical interannual variability of temperature and water vapor from a combined AIRS-MLS data set, J. Geophys. Res.-Atmos., 116, D06 103, https://doi.org/10.1029/2010JD014841, 2011.

Liess, S. and Geller, M. A.: On the relationship between QBO and distribution of tropical deep convection, J. Geophys. Res.-Atmos., 117, https://doi.org/10.1029/2011JD016317, 2012.

Lin, P., Paynter, D., Ming, Y., and Ramaswamy, V.: Changes of the tropical tropopause layer under global warming, J. Clim., 30, 1245–1258, https://doi.org/10.1175/JCLI-D-16-0457.1, 2017.

Livesey, N. J., Read, W. G., Wagner, P. A., Froidevaux, L., Lambert, A., Manney, G. L., Millán-Valle, L. F., Pumphrey, H. C., Santee, M. L., Schwartz, M. J., Wang, S., Fuller, R. A., Jarnot, R. F., Knosp, B. W., and Martinez, E.: Earth Observing System (EOS) Aura Microwave Limb Sounder (MLS), Version 4.2x Level 2 data quality and description document, Tech. Rep. JPL D-33509, Tech. Rep. version

4.2x-3.0, NASA Jet Propulsion Laboratory, 2017.

Mastenbrook, H.: Water-vapor measurements in the lower stratosphere, Can. J. Chem., 52, 1527–1531, https://doi.org/10.1139/v74-224, 1974.

Molod, A.: Constraints on the profiles of total water PDF in AGCMs from AIRS and a high-resolution model, J. Clim., 25, 8341–8352, https://doi.org/10.1175/JCLI-D-11-00412.1, 2012.

Molod, A., Takacs, L., Suarez, M., Bacmeister, J., Song, I.-S., and Eichmann, A.: The GEOS-5 atmospheric general circulation model: Mean climate and development from MERRA to Fortuna, Technical Report Series on Global Modeling and Data Assimilation Volume 28, NASA Goddard Space Flight Center, 2012.

Molod, A., Takacs, L., Suarez, M., and Bacmeister, J.: Development of the GEOS-5 atmospheric general circulation model: Evolution from MERRA to MERRA2, Geosci. Model Dev., 8, 1339, https://doi.org/10.5194/gmd-8-1339-2015, 2015.

Mote, P. W., Rosenlof, K. H., McIntyre, M. E., Carr, E. S., Gille, J. C., Holton, J. R., Kinnersley, J. S., Pumphrey, H. C., Russell, J. M., and Waters, J. W.: An atmospheric tape recorder: The imprint of tropical tropopause temperatures on stratospheric water vapor, J. Geophys. Res.-Atmos., 101, 3989–4006, https://doi.org/10.1029/95JD03422, 1996.

Murgatroyd, R. and Singleton, F.: Possible meridional circulations in the stratosphere and mesosphere, Q. J. Royal Meteorol. Soc., 87, 125–135, https://doi.org/10.1002/qj.49708737202, 1961.

Newell, R. E. and Gould-Stewart, S.: A stratospheric fountain?, J. Atmos. Sci., 38, 2789–2796, https://doi.org/10.1175/1520-0469(1981)038<2789:ASF>2.0.CO;2, 1981.

Oman, L., Waugh, D. W., Pawson, S., Stolarski, R. S., and Nielsen, J. E.: Understanding the changes of stratospheric water vapor in coupled Chemistry–Climate Model simulations, J. Atmos. Sci., 65, 3278–3291, https://doi.org/10.1175/2008JAS2696.1, 2008.

Oman, L. D. and Douglass, A. R.: Improvements in total column ozone in GEOSCCM and comparisons with a new ozone-depleting substances scenario, J. Geophys. Res.-Atmos., 119, 5613–5624, https://doi.org/10.1002/2014JD021590, 2014.

Pawson, S., Stolarski, R. S., Douglass, A. R., Newman, P. A., Nielsen, J. E., Frith, S. M., and Gupta, M. L.: Goddard Earth Observing System chemistry-climate model simulations of stratospheric ozone-temperature coupling between 1950 and 2005, J. Geophys. Res.-Atmos., 113, https://doi.org/10.1029/2007JD009511, 2008.

Pfister, L., Selkirk, H. B., Jensen, E. J., Schoeberl, M. R., Toon, O. B., Browell, E. V., Grant, W. B., Gary, B., Mahoney, M. J., Bui, T. V., and Hintsa, E.: Aircraft observations of thin cirrus clouds near the tropical tropopause, J. Geophys. Res.-Atmos., 106, 9765–9786, https://doi.org/10.1029/2000JD900648, 2001.

Ploeger, F., Konopka, P., Günther, G., Grooß, J.-U., and Müller, R.: Impact of the vertical velocity scheme on modeling transport in the tropical tropopause layer, J. Geophys. Res.-Atmos., 115, https://doi.org/10.1029/2009JD012023, 2010.

Plumb, R. A.: A "tropical pipe" model of stratospheric transport, J. Geophys. Res.-Atmos., 101, 3957–3972, https://doi.org/10.1029/95JD03002, 1996.

Plumb, R. A. and Bell, R. C.: A model of the quasi-biennial oscillation on an equatorial beta-plane, Q. J. Royal Meteorol. Soc., 108, 335–352, https://doi.org/

10.1002/qj.49710845604, 1982.

Randel, W. J. and Jensen, E. J.: Physical processes in the tropical tropopause layer and their roles in a changing climate, Nat. Geosci., 6, 169–176, https://doi.org/10.1038/ngeo1733, 2013.

Randel, W. J., Wu, F., and Gaffen, D. J.: Interannual variability of the tropical tropopause derived from radiosonde data and NCEP reanalyses, J. Geophys. Res.-Atmos., 105, 15 509–15 523, https://doi.org/10.1029/2000JD900155, 2000.

Randel, W. J., Wu, F., Oltmans, S. J., Rosenlof, K., and Nedoluha, G. E.: Interannual changes of stratospheric water vapor and correlations with tropical tropopause temperatures, J. Atmos. Sci., 61, 2133–2148, https://doi.org/10.1175/1520-0469(2004)061<2133:ICOSWV>2.0.CO;2, 2004.

Randel, W. J., Wu, F., Voemel, H., Nedoluha, G. E., and Forster, P.: Decreases in stratospheric water vapor after 2001: Links to changes in the tropical tropopause and the Brewer-Dobson circulation, J. Geophys. Res.-Atmos., 111, https://doi.org/10.1029/2005JD006744, 2006.

Read, W. G., Lambert, A., Bacmeister, J., Cofield, R. E., Christensen, L. E., Cuddy, D. T., Daffer, W. H., Drouin, B. J., Fetzer, E., Froidevaux, L., Fuller, R., Herman, R., Jarnot, R. F., Jiang, J. H., Jiang, Y. B., Kelly, K., Knosp, B. W., Kovalenko, L. J., Livesey, N. J., Liu, H., Manney, G. L., Pickett, H. M., Pumphrey, H. C., Rosenlof, K. H., Sabounchi, X., Santee, M. L., Schwartz, M. J., Snyder, W. V., Stek, P. C., Su, H., Takacs, L. L., Thurstans, R. P., Vömel, H., Wagner, P. A., Waters, J. W., Webster, C. R., Weinstock, E. M., and Wu, D. L.: Aura Microwave Limb Sounder upper tropospheric and lower stratospheric H_2O and relative humidity with respect to ice validation, J. Geophys. Res.-Atmos., 112, D24S35,

https://doi.org/10.1029/2007JD008752, 2007.

Robinson, G.: The transport of minor atmospheric constituents between troposphere and stratosphere, Q. J. Royal Meteorol. Soc., 106, 227–253, https://doi.org/10.1002/qj.49710644802, 1980.

Rodgers, C. D.: Inverse methods for atmospheric sounding: theory and practice, vol. 2, World scientific, 2000.

Rodgers, C. D. and Connor, B. J.: Intercomparison of remote sounding instruments, J. Geophys. Res.-Atmos., 108, https://doi.org/10.1029/2002JD002299, 2003.

Rosenlof, K. H.: Seasonal cycle of the residual mean meridional circulation in the stratosphere, J. Geophys. Res.-Atmos., 100, 5173–5191, https://doi.org/10.1029/94JD03122, 1995.

Russell, J. M., Gordley, L. L., Park, J. H., Drayson, S. R., Hesketh, W. D., Cicerone, R. J., Tuck, A. F., Frederick, J. E., Harries, J. E., and Crutzen, P. J.: The halogen occultation experiment, J. Geophys. Res.-Atmos., 98, 10 777–10 797, https://doi.org/10.1029/93JD00799, 1993.

Santer, B. D., Sausen, R., Wigley, T. M. L., Boyle, J. S., AchutaRao, K., Doutriaux, C., Hansen, J. E., Meehl, G. A., Roeckner, E., Ruedy, R., Schmidt, G., and Taylor, K. E.: Behavior of tropopause height and atmospheric temperature in models, reanalyses, and observations: Decadal changes, J. Geophys. Res.-Atmos., 108, https://doi.org/10.1029/2002JD002258, 2003.

Schiller, C., Grooß, J.-U., Konopka, P., Plöger, F., Silva dos Santos, F., and Spelten, N.: Hydration and dehydration at the tropical tropopause, Atmos. Chem. Phys., 9, 9647–9660, https://doi.org/10.5194/acp-9-9647-2009, 2009.

Schoeberl, M. and Dessler, A.: Dehydration of the stratosphere, Atmos. Chem.

Phys., 11, 8433–8446, https://doi.org/10.5194/acp-11-8433-2011, 2011.

Schoeberl, M., Dessler, A., and Wang, T.: Simulation of stratospheric water vapor and trends using three reanalyses, Atmos. Chem. Phys., 12, 6475–6487, https://doi.org/10.5194/acp-12-6475-2012, 2012.

Schoeberl, M., Dessler, A., and Wang, T.: Modeling upper tropospheric and lower stratospheric water vapor anomalies, Atmos. Chem. Phys., 13, 7783–7793, https://doi.org/10.5194/acp-13-7783-2013, 2013.

Schoeberl, M. R., Douglass, A. R., Zhu, Z., and Pawson, S.: A comparison of the lower stratospheric age spectra derived from a general circulation model and two data assimilation systems, J. Geophys. Res.-Atmos., 108, https://doi.org/10.1029/2002JD002652, 2003.

Schoeberl, M. R., Dessler, A. E., Wang, T., Avery, M. A., and Jensen, E. J.: Cloud formation, convection, and stratospheric dehydration, Earth Space Sci., 1, 1–17, https://doi.org/10.1002/2014EA000014, 2014.

Schwartz, M. J., Read, W. G., Santee, M. L., Livesey, N. J., Froidevaux, L., Lambert, A., and Manney, G. L.: Convectively injected water vapor in the North American summer lowermost stratosphere, Geophys. Res. Lett., 40, 2316–2321, https://doi.org/10.1002/grl.50421, 2013.

Seidel, D. J. and Randel, W. J.: Variability and trends in the global tropopause estimated from radiosonde data, J. Geophys. Res.-Atmos., 111, https://doi.org/10.1029/2006JD007363, 2006.

Shepherd, T. G.: Issues in stratosphere-troposphere coupling, J. Meteor. Soc. Japan, 80, 769–792, https://doi.org/10.2151/jmsj.80.769, 2002.

Sherwood, S. C. and Dessler, A. E.: On the control of stratospheric humidity, Geo-

phys. Res. Lett., 27, 2513–2516, https://doi.org/10.1029/2000GL011438, 2000.

Smalley, K. M., Dessler, A. E., Bekki, S., Deushi, M., Marchand, M., Morgenstern, O., Plummer, D. A., Shibata, K., Yamashita, Y., and Zeng, G.: Contribution of different processes to changes in tropical lower-stratospheric water vapor in chemistry–climate models, Atmos. Chem. Phys., 17, 8031–8044, https://doi.org/10.5194/acp-17-8031-2017, 2017.

Solomon, S., Rosenlof, K. H., Portmann, R. W., Daniel, J. S., Davis, S. M., Sanford, T. J., and Plattner, G.-K.: Contributions of stratospheric water vapor to decadal changes in the rate of global warming, Science, 327, 1219–1223, https://doi.org/10.1126/science.1182488, 2010.

Stenke, A. and Grewe, V.: Simulation of stratospheric water vapor trends: impact on stratospheric ozone chemistry, Atmos. Chem. Phys., 5, 1257–1272, https://doi.org/10.5194/acp-5-1257-2005, 2005.

Sun, Y. and Huang, Y.: An examination of convective moistening of the lower stratosphere using satellite data, Earth Space Sci., 2, 320–330, https://doi.org/10.1002/2015EA000115, 2015.

Tao, M., Konopka, P., Ploeger, F., Riese, M., Müller, R., and Volk, C. M.: Impact of stratospheric major warmings and the quasi-biennial oscillation on the variability of stratospheric water vapor, Geophys. Res. Lett., 42, 4599–4607, https://doi.org/10.1002/2015GL064443, 2015.

Ueyama, R., Jensen, E. J., Pfister, L., Diskin, G. S., Bui, T., and Dean-Day, J. M.: Dehydration in the tropical tropopause layer: A case study for model evaluation using aircraft observations, J. Geophys. Res.-Atmos., 119, 5299–5316, https://doi.org/10.1002/2013JD021381, 2014.

Ueyama, R., Jensen, E. J., Pfister, L., and Kim, J.-E.: Dynamical, convective, and microphysical control on wintertime distributions of water vapor and clouds in the tropical tropopause layer, J. Geophys. Res.-Atmos., 120, 10 483–10 500, https://doi.org/10.1002/2015JD023318, 2015.

Virts, K. S. and Houze, Jr., R. A.: Clouds and water vapor in the tropical tropopause transition layer over mesoscale convective systems, J. Atmos. Sci., 72, 4739–4753, https://doi.org/10.1175/JAS-D-15-0122.1, 2015.

Wang, T. and Dessler, A. E.: Analysis of cirrus in the tropical tropopause layer from CALIPSO and MLS data: A water perspective, J. Geophys. Res.-Atmos., 117, https://doi.org/10.1029/2011JD016442, 2012.

Wang, T., Randel, W., Dessler, A., Schoeberl, M., and Kinnison, D.: Trajectory model simulations of ozone (O_3) and carbon monoxide (CO) in the lower stratosphere, Atmos. Chem. Phys., 14, 7135–7147, https://doi.org/10.5194/acp-14-7135-2014, 2014.

Wang, W., Matthes, K., and Schmidt, T.: Quantifying contributions to the recent temperature variability in the tropical tropopause layer, Atmos. Chem. Phys., 15, 5815–5826, https://doi.org/10.5194/acp-15-5815-2015, 2015.

Waters, J. W., Froidevaux, L., Harwood, R. S., Jarnot, R. F., Pickett, H. M., Read, W. G., Siegel, P. H., Cofield, R. E., Filipiak, M. J., Flower, D. A., Holden, J. R., Lau, G. K., Livesey, N. J., Manney, G. L., Pumphrey, H. C., Santee, M. L., Wu, D. L., Cuddy, D. T., Lay, R. R., Loo, M. S., Perun, V. S., Schwartz, M. J., Stek, P. C., Thurstans, R. P., Boyles, M. A., Chandra, K. M., Chavez, M. C., Chen, G.-S., Chudasama, B. V., Dodge, R., Fuller, R. A., Girard, M. A., Jiang, J. H., Jiang, Y., Knosp, B. W., LaBelle, R. C., Lam, J. C., Lee, K. A., Miller, D., Oswald,

J. E., Patel, N. C., Pukala, D. M., Quintero, O., Scaff, D. M., Snyder, W. V., Tope, M. C., Wagner, P. A., and Walch, M. J.: The Earth observing system microwave limb sounder (EOS MLS) on the Aura satellite, IEEE Trans. Geosci. Remote Sens., 44, 1075–1092, https://doi.org/10.1109/TGRS.2006.873771, 2006.

WMO: Atmospheric Ozone 1985, World Meteorological Organization, 1986.

Wright, J., Fu, R., Fueglistaler, S., Liu, Y., and Zhang, Y.: The influence of summertime convection over Southeast Asia on water vapor in the tropical stratosphere, J. Geophys. Res.-Atmos., 116, https://doi.org/10.1029/2010JD015416, 2011.

Wright, J. S., Sobel, A. H., and Schmidt, G. A.: Influence of condensate evaporation on water vapor and its stable isotopes in a GCM, Geophys. Res. Lett., 36, https://doi.org/10.1029/2009GL038091, 2009.

Ye, H., Dessler, A. E., and Yu, W.: Effects of convective ice evaporation on interannual variability of tropical tropopause layer water vapor, Atmospheric Chemistry and Physics, 18, 4425–4437, 2018.

Yulaeva, E., Holton, J. R., and Wallace, J. M.: On the cause of the annual cycle in tropical lower-stratospheric temperatures, J. Atmos. Sci., 51, 169–174, https://doi.org/10.1175/1520-0469(1994)051<0169:OTCOTA>2.0.CO;2, 1994.

Zhou, C., Dessler, A., Zelinka, M., Yang, P., and Wang, T.: Cirrus feedback on interannual climate fluctuations, Geophys. Res. Lett., 41, 9166–9173, https://doi.org/10.1002/2014GL062095, 2014.